

UC Irvine

UC Irvine Previously Published Works

Title

Kinetics of the Reactions of CH₂O with Acetone, α -Diketones, and β -Diketones

Permalink

<https://escholarship.org/uc/item/3pv6h3xc>

Journal

The Journal of Physical Chemistry A, 125(39)

ISSN

1089-5639

Authors

Cornwell, Zachary A

Harrison, Aaron W

Murray, Craig

Publication Date

2021-10-07

DOI

10.1021/acs.jpca.1c05280

Copyright Information

This work is made available under the terms of a Creative Commons Attribution-NonCommercial-NoDerivatives License, available at

<https://creativecommons.org/licenses/by-nc-nd/4.0/>

Peer reviewed

Kinetics of the Reactions of CH₂OO with Acetone, α-Diketones, and β-Diketones

Zachary A. Cornwell,¹ Aaron W. Harrison,² and Craig Murray*,¹

1. *Department of Chemistry, University of California, Irvine, Irvine CA 92697, USA*

2. *Department of Chemistry, Austin College, Sherman, TX 75090, USA*

* Email: craig.murray@uci.edu; Telephone: +1-949-824-4218

Abstract

Rate constants for the reactions between the simplest Criegee intermediate, CH_2OO , with acetone, the α -diketones biacetyl and acetylpropionyl, and the β -diketones acetylacetone and 3,3-dimethyl-2,4-pentanedione have been measured at 295 K. CH_2OO was produced photochemically in a flow reactor by 355 nm laser flash photolysis of diiodomethane in the presence of excess oxygen. Time-dependent concentrations were measured using broadband transient absorption spectroscopy and the reaction kinetics were characterized under pseudo-first order conditions. The bimolecular rate constant for the $\text{CH}_2\text{OO} + \text{acetone}$ reaction is measured to be $(4.1 \pm 0.4) \times 10^{-13} \text{ cm}^3 \text{ s}^{-1}$ consistent with previous measurements. The reactions of CH_2OO with the β -diketones acetylacetone and 3,3-dimethyl-2,5-pentanedione are found to have broadly similar rate constants of $(6.6 \pm 0.7) \times 10^{-13} \text{ cm}^3 \text{ s}^{-1}$ and $(3.5 \pm 0.8) \times 10^{-13} \text{ cm}^3 \text{ s}^{-1}$, respectively; these values may be cautiously considered as upper limits. In contrast, α -diketones react significantly faster, with rate constants of $(1.45 \pm 0.18) \times 10^{-11} \text{ cm}^3 \text{ s}^{-1}$ and $(1.29 \pm 0.15) \times 10^{-11} \text{ cm}^3 \text{ s}^{-1}$ measured for biacetyl and acetylpropionyl. The potential energy surfaces for these 1,3-dipolar cycloaddition reactions are characterized at the M06-2X/aug-cc-pVTZ and CBS-QB3 levels of theory and provide additional support to the observed experimental trends. The reactivity of carbonyl compounds with CH_2OO is also interpreted by application of frontier molecular orbital theory and predicted using Hammett substituent constants. Finally, the results are compared with other kinetics studies of Criegee intermediate reactions with carbonyl compounds and discussed within the context of their atmospheric relevance.

Introduction

Carbonyl oxides, known as Criegee intermediates (CIs), are formed by alkene ozonolysis reactions and are important reactive species in the troposphere.¹⁻⁵ It is now well-established that ozonolysis of alkenes proceeds in the gas-phase via the cycloaddition mechanism originally proposed by Criegee,⁶ after whom the intermediates are named. Initial cycloaddition forms a five-membered cyclic primary ozonide, which rapidly decomposes into a carbonyl and a carbonyl oxide. The energized CI subsequently either decomposes or is collisionally relaxed to form a stabilized CI. A broad range of alkenes are found in the troposphere, and consequently a great variety of CIs are thought to be formed in the atmosphere.⁴ Depending on the substituents and the particular stereoisomer formed, CIs can themselves undergo thermal unimolecular decomposition or react with trace atmospheric gases. For larger CIs, unimolecular decomposition is thought to be the dominant sink.⁷ For the simplest CI, formaldehyde oxide (CH_2OO), unimolecular decomposition is slow, and secondary reactions are more significant. Globally, reaction with water dimer is the dominant mechanism for removing CH_2OO ,⁸ although other trace species, such as organic or inorganic acids, with large CI reaction rate constants, can be locally competitive.⁹⁻¹²

Previous work has examined gas-phase reactions between CIs and carbonyl compounds produced in alkene ozonolysis reactions,¹³⁻²⁰ and using photochemical production.²¹⁻²⁴ In the Criegee mechanism for ozonolysis, decomposition of the primary ozonide yields a carbonyl oxide and an aldehyde or ketone, which can subsequently react to form a secondary ozonide (SOZ, a 1,2,4-trioxolane). Moortgat and co-workers demonstrated that the presence of additional carbonyls led to formation of the expected SOZs in the gas phase ozonolysis of ethene of using Fourier transform infrared spectroscopy (FTIR) for product detection.¹⁴⁻¹⁶ A subsequent study found that hexafluoroacetone (HFA) reacted ~ 13 times faster with CH_2OO than does acetaldehyde at 730 Torr and 295 K.¹⁷ Fenske *et al.* also used FTIR to monitor SOZ production from acetone oxide (CH_3CHOO), produced by

ozonolysis of *trans*-2-butene, reacting with acetaldehyde and estimated a rate constant of $1.1 \times 10^{-12} \text{ cm}^3 \text{ s}^{-1}$ (with a factor of six accuracy).¹⁸ Tobias and Ziemann determined reactivity trends for reactions of the C13 CI formed from ozonolysis of 1-tetradecene using real-time thermal desorption particle beam mass spectrometry.¹⁹ The observed reactivity trends indicated that HCHO reacted with the C13 CI around 50–100 times faster than alcohols such as methanol and isopropanol,^{25,26} implying rate constants on the order $10^{-11} \text{ cm}^3 \text{ s}^{-1}$. In addition, Berndt *et al.* used ozonolysis to form CH₂OO in a flow reactor and monitored concentrations by titrating with SO₂ and detecting the H₂SO₄ product by chemical ionization mass spectrometry (CIMS).²⁰ Rate constants of $(1.7 \pm 0.5) \times 10^{-12} \text{ cm}^3 \text{ s}^{-1}$ and $(3.4 \pm 0.9) \times 10^{-13} \text{ cm}^3 \text{ s}^{-1}$ were measured at 1 atm and 297 K for the reactions of CH₂OO with acetaldehyde and acetone, respectively.

Recently, photochemical routes involving reactions of α -iodoalkyl radicals with oxygen have been used to generate higher yields of carbonyl oxides and facilitate direct detection using absorption spectroscopy and photoionization techniques.^{27,28} Several groups have used direct methods to investigate the kinetics of reactions of CH₂OO with carbonyl compounds. Taatjes *et al.* used tunable synchrotron photoionization mass spectrometry (PIMS) to directly measure CH₂OO loss rates in the reactions of CH₂OO with acetone, acetaldehyde, and HFA to be $(2.3 \pm 0.3) \times 10^{-13} \text{ cm}^3 \text{ s}^{-1}$, $(9.5 \pm 0.7) \times 10^{-13} \text{ cm}^3 \text{ s}^{-1}$, $(3.0 \pm 0.3) \times 10^{-11} \text{ cm}^3 \text{ s}^{-1}$, respectively, at a pressure of 4 Torr and a temperature of 295 K.²¹ Secondary ozonides were observed in the mass spectra as products of the ketone reactions, although not of the acetaldehyde reaction. Subsequently, Elsamra *et al.* determined rate constants for acetone and acetaldehyde as $(3.0 \pm 0.6) \times 10^{-13} \text{ cm}^3 \text{ s}^{-1}$ and $(1.2 \pm 0.2) \times 10^{-12} \text{ cm}^3 \text{ s}^{-1}$ at 25 Torr and 298 K using multi-pass absorption spectroscopy.²³ Weak negative temperature and positive pressure dependences were observed. Stone *et al.* also examined the kinetics of the CH₂OO + acetaldehyde reaction.²² In that study, CH₂OO was generated photochemically, but the reaction was probed indirectly by monitoring the HCHO products of SO₂ decomposition using laser-induced fluorescence (LIF). The HCHO yield was found to decrease significantly with increasing pressure (from 88% at 4

Torr to only 4% at 730 Torr) due to stabilization of the SOZ, explaining the absence of SOZ signal in the low-pressure PIMS measurements.²¹ The rate constant for the acetaldehyde reaction in the high-pressure limit was estimated to be $\sim 1.7 \times 10^{-12} \text{ cm}^3 \text{ s}^{-1}$, consistent with the direct measurements. Recently, Eskola *et al.* have used PIMS to explore the kinetics and mechanism of the CH₂OO reactions with methyl vinyl ketone (MVK) and methacrolein (MACR).²⁴ These unsaturated carbonyls are, along with CH₂OO, important products of isoprene ozonolysis. The rate constants at 300 K and 4 Torr were found to be $(5.0 \pm 0.2) \times 10^{-13} \text{ cm}^3 \text{ s}^{-1}$ for MVK and $(4.4 \pm 0.5) \times 10^{-13} \text{ cm}^3 \text{ s}^{-1}$ for MACR. SOZ products were observed in the mass spectra and confirmed that the addition occurs primarily via 1,3-dipolar cycloaddition at the carbonyl site rather than the olefinic site, consistent with measurements of much smaller rate constants ($\sim 10^{-15} \text{ cm}^3 \text{ s}^{-1}$) for reactions of CH₂OO with various alkenes.²⁹

Theoretical studies have also explored CI reactions with carbonyl compounds, particularly the CH₂OO + HCHO reaction. Cremer *et al.*³⁰ identified a dipole-dipole complex in the reaction of formaldehyde and formaldehyde oxide, which suggested the reactants would orient to promote cycloaddition to form the SOZ. The complex and transition states were subsequently characterized at various levels of theory by Aplincourt and Ruiz-López,^{31,32} who performed calculations to explore mechanisms that led to formic acid anhydride and carboxylic acid formation in the atmosphere. For the reaction of CH₂OO with formaldehyde, calculations at the CCSD(T) level found the entrance channel van der Waals (vdW) complex to lie 5.8 kcal mol⁻¹ lower in energy than the reactants, with a small, submerged barrier of $\sim 1.2 \text{ kcal mol}^{-1}$ leading to formation of the SOZ in a process that is exothermic by $-49.0 \text{ kcal mol}^{-1}$. Elsamra *et al.* described the steps leading to the formation of the SOZ as two transition states: a loose outer transition state (TS_{outer}) for the formation of the vdW complex and an inner 1,3-cycloaddition transition state (TS_{inner}) to form the SOZ. It was shown that either of the transition states could be rate-limiting depending on the temperature.²³ Jalan *et al.* found SOZ formation to increase in the order HCHO < CH₃CHO < CH₃COCH₃.³³

In this work, we describe the results of flash photolysis broadband transient absorption spectroscopy experiments exploring the kinetics of gas phase reactions of CH_2OO with acetone, the α -diketones 2,3-butanedione (biacetyl, BiAc) and 2,3-pentanedione (acetylpropionyl, AcPr), and the β -diketones 2,4-pentanedione (acetylacetone, AcAc) and 3,3-dimethyl-2,4-pentanedione (dMAcAc) (see Figure 1). The α -diketone reactions are found to be 20–40 times faster than those of acetone and β -

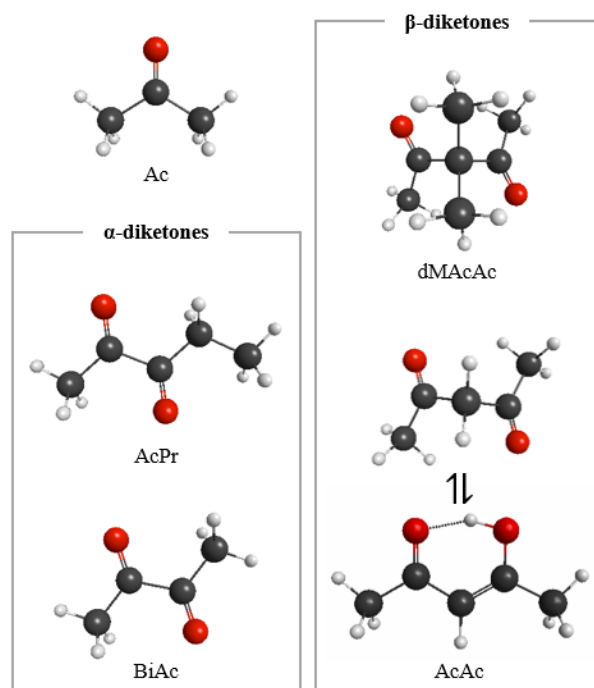


Figure 1 Acetone (2-propanone, Ac), the α -diketones acetylpropionyl (2,3-pentanedione, AcPr) and biacetyl (2,3-butanedione, BiAc); and the β -diketones acetylacetone (2,4-pentanedione, AcAc) and 3,3-dimethyl-2,4-pentanedione (dMAcAc). The enolone and diketone tautomers of AcAc are both shown but the former is predominant in the gas phase.

diketones. Complementary *ab initio* calculations are used to elucidate the detailed reaction mechanisms and identify a correlation between frontier orbital energy gaps and the experimental rate constants. A strong correlation is also demonstrated between rate constants for CH_2OO + carbonyl reactions and Hammett substituent constants.

Experimental and computational methods

The flow reactor apparatus used to study the kinetics of Criegee intermediate reactions has been described in detail previously.^{10,26,34} Briefly, CH₂O was produced in a 100 cm long stainless steel flow reactor by photolysis of CH₂I₂ in the presence of excess O₂ and its time-dependent concentration was measured using broadband transient absorption spectroscopy. The 355 nm output of a Nd:YAG laser (Continuum Surelite II-10, 10 Hz repetition rate) was attenuated to provide ~8 mJ photolysis pulses (fluences of approximately ~30 mJ cm⁻²). Transient absorption spectra were recorded in the wavelength range 360–400 nm using 500 ns duration pulses from a broadband UV LED (LightSpeed Technologies), which were dispersed in a spectrograph (Andor Shamrock 303i with iDus 420 CCD camera). Transient spectra were typically recorded at fifteen delay times ($\Delta t = t_{\text{LED}} - t_{\text{photolysis}}$), each derived from the average of 300 reference and signal spectra. Reference spectra were recorded with $\Delta t = -10 \mu\text{s}$ (i.e. the LED pulse passes through the cell 10 μs before the photolysis laser). Custom data acquisition software (National Instruments LabVIEW) controls a digital delay generator (Quantum Composers 9528), which provides triggers for the laser, the LED driver, and the CCD camera, and processes raw data to generate the transient absorption spectra.

Gas flow rates into the reactor were controlled using choked-flow orifices (O'Keefe). N₂ (Praxair, 5.0 UHP) and O₂ (Airgas, 4.4 UHP) were passed through drying filters to ensure removal of residual water vapor before entering the cell. The Criegee intermediate precursor, CH₂I₂, and the carbonyl reactants are liquids at room temperature and were kept in smog bubblers (Ace Glass), which were immersed in a water bath maintained at 295 K in order to stabilize the vapor pressure and prevent evaporative cooling of the liquid. The equilibrium vapor of each reactant [Ac: 200 Torr; BiAc: 48 Torr; AcPr: 21 Torr; AcAc: 5 Torr; dMAcAc: 3 Torr (all Sigma-Aldrich, reagent grade)]³⁵ was carried into the reactor by a flow of N₂ at a total pressure of 5 psig (1020 Torr). Experiments using BiAc were performed with the smog bubbler immersed in an ice bath at 273 K, which reduces the vapor pressure to 13

Torr. A range of choked-flow orifices were used to control reactant concentrations, which were quantified by absorbance measurements as described below. All kinetics measurements were performed under pseudo-first order conditions of excess carbonyl compound. A small flow of nitrogen (30 sccm) was used to purge the windows and minimize formation of residue on the surfaces. An independent flow of N₂ was controlled via an adjustable tap to maintain constant total pressure. Typical total flow rates were ~3.2 sLpm, which resulted in a static pressure of ~67 Torr (~2.2×10¹⁸ cm³) in the flow reactor, the majority of which was N₂ (~1.9×10¹⁸ cm³). The same CH₂I₂ and O₂ flow rates were used for all kinetics measurements and led to estimated concentrations of ~5.5×10¹⁴ cm⁻³ and ~2.1×10¹⁷ cm⁻³, respectively. At least four independent measurements of the reaction kinetics were made for each carbonyl; the choked-flow orifices that controlled the reactant concentration were used in random order for each run to minimize systematic errors, such as deterioration of the windows.

UV/visible absorption spectra of the carbonyls were measured over the range 200–700 nm in a commercial spectrophotometer (Agilent, Cary 60 UV-Vis). A few drops of the liquids were placed in a capped quartz cuvette and the liquid/vapor mixture was allowed to reach equilibrium, which was confirmed by repeated measurements showing that the absorbance was constant with time. Absorption spectra of the carbonyl compounds were recorded in the flow reactor using LEDs centered at 420 nm and at 280 nm over the same range of reactant/N₂ flow rates used for the kinetics measurements.

Electronic structure calculations of the unimolecular reaction intermediates and energies involved were performed with the Gaussian 16³⁶ and GAMESS^{37–39} programs. Equilibrium and transition state structures were optimized with the M06-2X hybrid functional⁴⁰ using the Dunning-type cc-pVTZ basis set augmented with diffuse functions (aug-cc-pVTZ). Minima and transition states were confirmed by frequency analysis and by following the intrinsic reaction coordinate (IRC). The structures obtained at the M06-2X/aug-cc-pVTZ level of theory were then used as input for

calculations with the CBS-QB3 compound method.⁴¹ These levels of theory were chosen as they have been shown to provide reliable thermochemistry and geometries for reactions involving the main group elements at modest computational cost.⁴²⁻⁴⁴ Cartesian coordinates and images of the optimized geometries of the entrance channel complex intermediates, transition states, and secondary ozonide products for the BiAc and AcAc reactions (calculated at the M06-2X/aug-cc-pVTZ level) can be found in the Supporting Information.

Results

1. Reactant absorption spectroscopy and calibration

In contrast to the acids and alcohols studied previously,^{10,26} the carbonyl species have absorption features that overlap with available UV LEDs and the concentrations obtained under typical experimental conditions can be directly quantified. Figure 2 shows gas phase absorption spectra for all the reactants measured in a Cary-60 spectrometer over the wavelength range 225–475 nm at 295 K. Absolute absorption cross sections were determined from application of the Beer-Lambert law, assuming equilibrium vapor pressures for each compound.³⁵ The measured cross sections were found to be in excellent agreement with previously reported values, where available.⁴⁵ The α -diketones AcPr and BiAc have similar absorption spectra, featuring bands in the visible and UV. The visible bands are almost identical for BiAc and AcPr, with peak absorption cross sections $\sim 7 \times 10^{-20}$ cm² and irregular vibrational structure. The UV band of BiAc is weaker than the visible band with a peak absorption of $\sim 5 \times 10^{-20}$ cm² at 271 nm. Diffuse, regular vibrational structure can be seen across the UV band. The equivalent band in the AcPr spectrum appears as a shoulder, overlapping a stronger band at 251 nm that can be assigned to the enolone tautomer that is estimated with the aid of TDDFT calculations to be present at $\sim 0.03\%$. In contrast, the absorption spectra of the β -diketone absorption spectra have no bands in the visible. AcAc absorption is primarily due to the predominant enolone tautomer. The exceptionally large peak absorption cross section for AcAc (Messaadia *et al.*⁴⁶

report $4.6 \times 10^{-17} \text{ cm}^2$ at 262 nm) precludes measurement at the equilibrium vapor pressure ($A > 4$). The dMAcAc spectrum appears to be qualitatively the same shape as the UV band of AcPr, albeit the maximum cross section is larger ($5 \times 10^{-19} \text{ cm}^2$) and the absorption peak at 268 nm is shifted $\sim 15 \text{ nm}$ to longer wavelength. The lack of H-atoms on the central carbon atom in dMAcAc should prevent tautomerization.

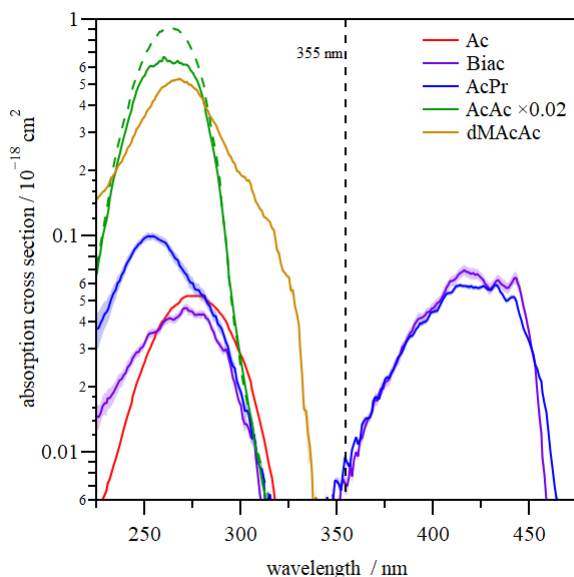


Figure 2 Gas phase absorption spectra at 295 K of acetone, BiAc, AcPr, AcAc, and dMAcAc. The AcAc absorption cross section values have been reduced by a factor of fifty; the dashed line is the measurement of Messaadia *et al.*,⁴⁶ which captures the peak absorption. Shaded areas are 1σ uncertainties from repeated measurements.

In our previous kinetics studies,^{10,26} the reactant concentrations, in cm^{-3} , were estimated using

$$[X]_{\text{est}} = \chi F P_{\text{tot}} \frac{N_A}{10^3 RT} \quad (\text{E1})$$

where χ is the mole fraction of carbonyl compound X in the X/N₂ flow, F is the fractional contribution of the X/N₂ to the total gas flow as determined from the choked-flow orifice specifications, and P_{tot} is

the total pressure in the reactor, which was maintained at a constant value of 67 ± 1 Torr for all experiments. N_A is the Avogadro constant in mol^{-1} , $R = 62.364 \text{ L Torr}^{-1} \text{ mol}^{-1} \text{ K}^{-1}$ is the gas constant, and T is the temperature in K. Calibration measurements for each reactant were made by recording absorption spectra in the flow reactor using the same collections of choked-flow orifices to vary the concentration as in the kinetics measurements (see below). Experimental concentrations $[X]_{\text{exp}}$ were determined using the absorption cross sections shown in Figure 2 and used to construct calibration

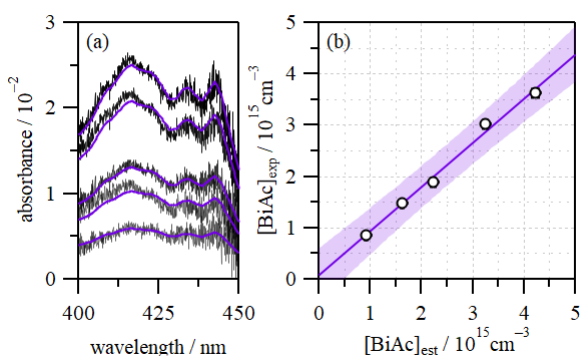


Figure 3 (a) Typical experimental absorbances (black) due to BiAc measured using the same selection of choked-flow orifice as in the kinetics experiments. Best-fit scaled BiAc absorption spectra are also shown (purple). (b) Calibration plot of measured concentrations, $[\text{BiAc}]_{\text{exp}}$, determined from the spectra plotted against estimated concentrations, $[\text{BiAc}]_{\text{est}}$. The gradient, $[\text{BiAc}]_{\text{exp}}/[\text{BiAc}]_{\text{est}} < 1$, indicates that reactant concentrations are slightly over-estimated. The shaded area is a 2σ prediction band.

plots. Absorption measurements were repeated at least four times for each reactant to ensure repeatability and quantify uncertainties.

As an example, Figure 3(a) shows BiAc absorption spectra recorded in the flow reactor using a visible LED centered at 420 nm. Equivalent measurements were made for AcPr, also using the 420 nm LED, while an LED centered at 280 nm was used for Ac, AcAc, and dMAcAc. The relationship between the measured and estimated concentrations is linear, as shown in Figure 3(b). In general, the use of

equation (E1) was found to systematically *over*-estimate the reactant concentrations: $[X]_{\text{exp}}/[X]_{\text{est}} < 1$ with an average value of 0.91 ± 0.10 . The origin of the discrepancy is not clear, but presumably results from surface losses as the reactant/ N_2 gas mixture passes through the gas manifold into the flow reactor. The calibration factors $[X]_{\text{exp}}/[X]_{\text{est}}$ for each reactant are compiled in Table 1 and used to scale the estimated reactant concentrations in the kinetics measurements.

Table 1 Reactant vapor pressures ($P_{\text{vap},X}$), bimolecular rate constants derived using experimental ($k_{X,\text{exp}}$) reactant number densities, and ratio of experimentally measured reactant concentrations to those estimated ($[X]_{\text{exp}}/[X]_{\text{est}}$). The asterisk on the value of $P_{\text{vap,BiAc}}$ indicates that the liquid sample was held at 273 K rather than 295 K. All reported rate constants were derived from the *overall* fits of the experimental data (see text). The results of alternative analyses are compiled in the Supporting Information. Uncertainties are 1σ .

	$P_{\text{vap},X} / \text{torr}$	$k_{X,\text{exp}} / 10^{-13} \text{ cm}^3 \text{ s}^{-1}$	$[X]_{\text{exp}}/[X]_{\text{est}}$
Ac	200.5	4.07 ± 0.43	0.87 ± 0.05
BiAc	13.4*	145 ± 18	0.94 ± 0.12
AcPr	21.2	129 ± 15	0.84 ± 0.10
AcAc	5.4	6.59 ± 0.68	0.94 ± 0.10
dMAcAc	3.4	3.54 ± 0.79	0.97 ± 0.09

2. Transient absorption spectroscopy

CH_2OO was produced following the 355 nm photolysis of CH_2I_2 in the presence of excess O_2 and its time dependent concentration determined from analysis of transient absorption spectra recorded at

various time delays after photolysis. In the absence of any additional reactants, CH₂OO is thought to be formed and removed by the following reaction sequence, based on the model described by Ting *et al.*⁴⁷



In the presence of excess O₂, the CH₂I + O₂ reaction is fast (1.4×10⁻¹² cm³ s⁻¹) and rapidly converts photolytically generated iodomethyl radicals to CH₂OO.⁴⁸ At a total pressure of 67 Torr, the fractional yield of CH₂OO via reaction (R2a) is estimated to be approximately 0.69.^{47,49} Typically, maximum CH₂OO concentrations of ~2.5×10¹³ cm⁻³ are reached approximately 10 μs after photolysis. Formation of the iodomethylperoxy adduct CH₂IO₂ via reaction (R2c) accounts for most of the remaining products, while reaction (R2b) is a minor channel.⁵⁰ The self-reaction (R4) is fast and is primarily responsible for loss of CH₂OO in the absence of other reactants.^{47,51-53} In the analysis that follows, we hold the rate constant for CH₂OO self-reaction fixed. Under the current experimental conditions, diffusion and wall losses of CH₂OO are negligible and thermal unimolecular decomposition is too slow to significantly contribute to its loss rate.^{7,53}

Figure 4(a) shows representative transient absorption spectra recorded at three delays (10 μs, 70 μs, and 300 μs) in the absence of any additional reactant. Absorbance in the 362–395 nm spectral region

is due to CH₂OO and IO. A small fraction of the IO is formed directly by reaction (R2b), while the majority is due to the secondary reaction (R3).^{47,50} The characteristic vibronic band progression^{34,54,55} of CH₂OO, is evident at the shortest delay, but becomes increasingly indistinct at longer delays at which time the spectra increasingly resemble that of IO.⁵⁶ The transient absorption

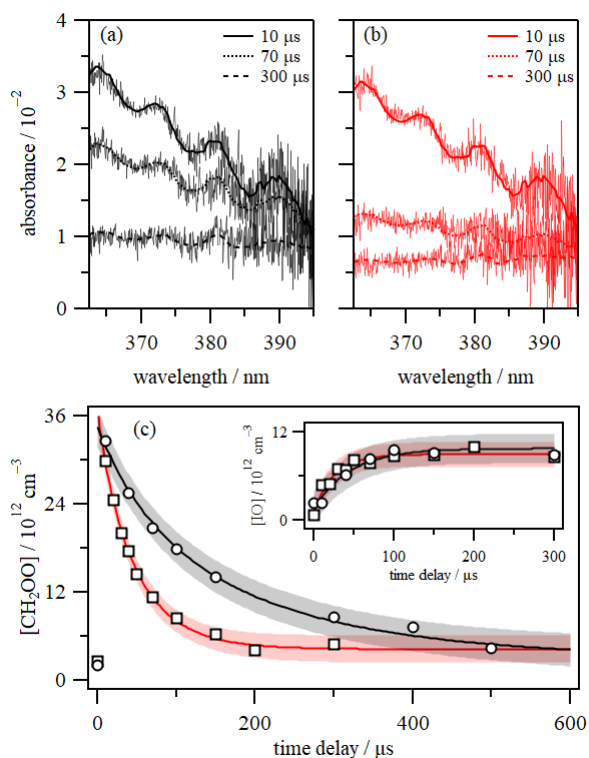


Figure 4 Broadband transient absorption spectra, recorded over the range 365–390 nm at the indicated time delays after photolysis (a) in the absence of any reactant and (b) in the presence of $[Ac]_{\text{exp}} = 2.47 \times 10^{16} \text{ cm}^{-3}$. (c): Time-dependent concentration profiles for CH₂OO and IO (inset) derived from the transient absorption spectra.

spectra shown in Figure 4(b) were recorded at the same time delays but with $[Ac]_{\text{exp}} \approx 2.5 \times 10^{16} \text{ cm}^{-3}$. The spectrum recorded at a delay of 10 μs is almost identical to that in Figure 4(a), indicating that the presence of Ac has no significant effect on the CH₂OO formation kinetics. The 70 μs and 300 μs spectra in Figure 4(a) and (b) are distinctly different, however, and show that CH₂OO is removed

more rapidly in the presence of Ac. The transient absorption spectra are decomposed by fitting to a linear combination of wavelength-dependent CH₂OO and IO absorption cross sections, $\sigma(\lambda)$,^{35,54} to yield time-dependent concentrations for each absorber:

$$\frac{A(\lambda)}{l} = [\text{CH}_2\text{OO}]\sigma_{\text{CH}_2\text{OO}}(\lambda) + [\text{IO}]\sigma_{\text{IO}}(\lambda) \quad (\text{E2})$$

Here, l is the 100 cm path length of the flow reactor. The concentration profiles of both CH₂OO and IO derived from the transient absorption spectra are shown in Figure 4(c). The [CH₂OO]_{*t*} profile shows an increased loss rate in the presence of Ac but the peak concentrations observed at short delays are unaffected, indicating that the carbonyl reactant does not noticeably affect the chemistry leading to CH₂OO production. The [IO]_{*t*} profiles are not affected by the presence of Ac; both the rise time and maximum concentration reached before slow removal by self-reaction are indistinguishable. These observations hold for all reactants (and reactant concentrations) used in the experiments.

CH₂OO loss rates are quantified using a simplified kinetic model that includes second order loss due to self-reaction (with rate constant k_{self}) and other processes that are assumed to follow first order (or pseudo-first order) kinetics (rate constant k_{loss}). The differential rate equation for the CH₂OO concentration is written as

$$\frac{d[\text{CH}_2\text{OO}]}{dt} = -2k_{\text{self}}[\text{CH}_2\text{OO}]^2 - k_{\text{loss}}[\text{CH}_2\text{OO}] \quad (\text{E3})$$

where

$$k_{\text{loss}} = k_{\text{bgd}} + k_{\text{X}}[\text{X}] \quad (\text{E4})$$

is the observed loss rate, which is partitioned between pseudo-first order loss due to reaction with carbonyl species X with rate constant k_{X} and the phenomenological background loss rate, k_{bgd} , that is observed in the absence of any carbonyl compound. Equation (E3) can be solved analytically to yield

the integrated rate equation:

$$[\text{CH}_2\text{OO}]_t = \frac{k_{\text{loss}}[\text{CH}_2\text{OO}]}{k_{\text{loss}} \exp(k_1 t) - 2k_{\text{self}}[\text{CH}_2\text{OO}][1 - \exp(k_{\text{self}} t)]} \quad (\text{E5})$$

Experimental concentration-time profiles are fit to Equation (E5) to extract k_{loss} with k_{self} constrained to the value of $7.4 \times 10^{-11} \text{ cm}^3 \text{ s}^{-1}$ reported by Chhantyal-Pun *et al.*⁵³ The values of k_{loss} obtained from the fits are insensitive to the precise value of k_{self} chosen. A re-analysis of a subset of the experimental data using the JPL recommended value⁵⁷ of $7.12 \times 10^{-11} \text{ cm}^3 \text{ s}^{-1}$ had only a very modest effect on the values of k_{loss} , and a negligible effect on the bimolecular rate constants. Examples of the typical quality of the fits to the experimental data obtained using Equation (E5) can be seen in Figure 4(c).

Rate constants were measured under pseudo-first order conditions of excess carbonyl reactant. Each experimental run involved measurements at five concentrations that spanned the range 10^{14} – 10^{17} cm^{-3} . With the exception of Ac, discussed in detail below, the loss rates were observed to increase linearly with the reactant concentration. The concentration range was constrained somewhat by the reaction rates, the available choked-flow orifices, the reactant vapor pressures, and the need to maintain constant total pressure in the flow reactor. Measurements were repeated at least four times for each reaction to ensure repeatability and to quantify the experimental uncertainties. Rate constants were obtained by simultaneously fitting the *overall* data sets to equation (E4) to extract values of k_{bgd} and k_{x} . In addition to fitting the *overall* data sets, two other approaches were also adopted. First, independent linear fits were performed for each *individual* experimental run, and the results averaged. Second, after noting that in most experiments, the variance in k_{x} was typically much smaller than that in k_{bgd} , individual kinetics runs were fit simultaneously, allowing k_{bgd} to vary independently, but returning a single *global* value of k_{x} . All three fitting approaches (*overall*, *individual*, and *global*) yielded consistent values for k_{bgd} and k_{x} . Only the values obtained from the *overall* fits are discussed in the text and summarized in Table 1. The results of the *individual* and *global* fitting approaches and the statistical uncertainties arising from the linear least-squares fitting

are compiled in the Supporting Information.

The $[X]_{\text{exp}}/[X]_{\text{est}}$ ratios determined from repeated measurements for each reactant are also compiled in Table 1, alongside rate constants, $k_{X,\text{exp}}$. While the uncertainties in $[X]_{\text{exp}}/[X]_{\text{est}}$ are relatively small, they are typically larger than the statistical uncertainties resulting from either data fitting or among the individual measurements of k_1 . For each reaction rate constant, the reported uncertainty (1σ) is based on the larger of the relative uncertainties arising from the fitting or the concentration

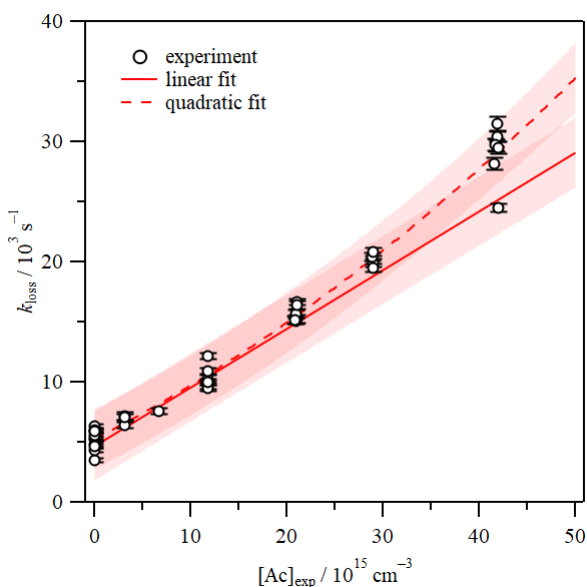


Figure 5 Observed pseudo-first order loss rates (symbols), and linear (solid line) and quadratic fits (dashed line) for the reaction of CH₂OO with Ac at 295 K and 67 Torr. The shaded areas represent 2 σ prediction bands.

calibration factor (~10–20%).

The pseudo-first order loss rates observed for the CH₂OO + Ac reaction are plotted as a function of the estimated Ac concentrations in Figure 5. Fitting the *overall* data set, which comprises five individual kinetic runs, to Equation (E4) yields $k_{\text{Ac}} = (5.6 \pm 0.3) \times 10^{-13} \text{ cm}^3 \text{ s}^{-1}$, which is ~40% larger than previous measurements.^{20,21,23} While equation (E4) provides a plausible fit to the data the relatively high concentrations of [Ac] and slight curvature evident in Figure 5, suggests an additional

contribution to the loss rate from acetone dimer, Ac_2 . Using data from Anderson *et al.*,⁵⁸ the equilibrium constant for formation of acetone dimer at 295 K is $K_p = 0.098 \text{ atm}^{-1}$ ($K_c = 4.2 \times 10^{-21} \text{ cm}^3$), leading to dimer concentrations $[Ac_2] = 4.1 \times 10^{10} \text{ cm}^{-3}$ to $7.5 \times 10^{12} \text{ cm}^{-3}$ (or 13–177 ppm). While these concentrations are low, acetone dimer may contribute to CH_2OO loss if the reaction rate constant is sufficiently large relative to that of the monomer reaction. Consequently, we include an additional term $k_{Ac_2}[Ac_2]$ to equation (E4), leading to

$$k_{\text{loss}} = k_{\text{bgd}} + k_{Ac}[Ac] + k_{Ac_2}K_c[Ac]^2 \quad (\text{E6})$$

where

$$[Ac_2] = K_c[Ac]^2 \quad (\text{E7})$$

Fitting to the quadratic equation (E6) yields an improved fit (shown in Figure 5) with $k_{Ac} = (4.1 \pm 0.4) \times 10^{-13} \text{ cm}^3 \text{ s}^{-1}$ and $k_{Ac_2}K_c = (3.9 \pm 1.0) \times 10^{-30} \text{ cm}^6 \text{ s}^{-1}$, with the former rate constant agreeing well with previous measurements for the $CH_2OO + Ac$ reaction.^{20,21,23} At the upper end of the $[Ac]$ range, the dimer reaction is responsible for up to 30% of the total CH_2OO loss while at the lower end of the range (specifically $[Ac] < 10^{16} \text{ cm}^{-3}$ i.e. the range of concentrations used for the other reactions discussed below) the dimer contribution is at most a few %.

Although imprecisely determined, the value obtained for $k_{Ac_2}K_c$ suggests an extremely large rate constant of $(9.2 \pm 2.4) \times 10^{-10} \text{ cm}^3 \text{ s}^{-1}$ for the $CH_2OO + Ac_2$ reaction. By comparison, reaction of CH_2OO with water dimer is indeed much faster than the monomer. However, the reaction mechanism involves direct participation of both water molecules in the transition state resulting in a much higher rate via an autocatalytic mechanism. In the case of acetone dimer, there is less reason to expect the dimer to react much more rapidly than the monomer. It is possible that the presence of the second acetone molecule could stabilize the cycloaddition transition state to some extent resulting in an increased reaction rate.

Figure 6 shows the analogous pseudo-first order loss rates observed for the $\text{CH}_2\text{OO} + \text{BiAc}$, AcPr , AcAc , and dMAcAc reactions, alongside linear fits to equation (E4). The α -diketone reactions have rate constants that are far larger than acetone. Based on the *overall* fits to the complete data sets we find for the α -diketones that $k_{\text{BiAc}} = (1.45 \pm 0.18) \times 10^{-11} \text{ cm}^3 \text{ s}^{-1}$ and $k_{\text{AcPr}} = (1.29 \pm 0.15) \times 10^{-11} \text{ cm}^3 \text{ s}^{-1}$. In contrast, the rate constants for the β -diketones are similar in magnitude to that of acetone with values of $k_{\text{AcAc}} = (6.2 \pm 0.5) \times 10^{-13} \text{ cm}^3 \text{ s}^{-1}$ and $k_{\text{dMAcAc}} = (3.4 \pm 0.8) \times 10^{-13} \text{ cm}^3 \text{ s}^{-1}$. For the β -diketone reactions,

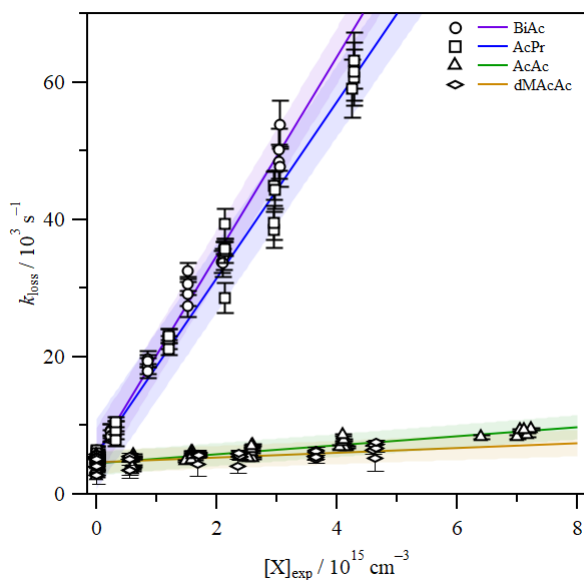
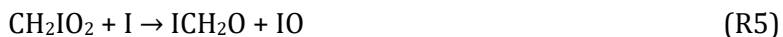


Figure 6 Observed pseudo-first order loss rates (symbols) and fits (lines) for the reaction of CH_2OO with BiAc (circle, purple), AcPr (square, blue), AcAc (triangle, green) and dMAcAc (diamond, yellow) at 295 K and 67 Torr. The shaded areas represent 2σ prediction bands.

the limited range of reactant concentrations restricted the maximum observed loss rates to only $\sim 1.5\text{--}2 \times k_{\text{bgd}}$ and the rate constants may be better considered cautiously as upper limits. The range of reactant concentrations used are much smaller, with $[X] < 8 \times 10^{15} \text{ cm}^{-3}$. Under these conditions, any contributions to the observed CH_2OO loss from dimers are expected to be negligible and no curvature is observed in the pseudo-first order plots.

3. Modeling and systematic uncertainties in k_{loss}

To explore the robustness of determining k_{loss} by fitting $[\text{CH}_2\text{OO}]_t$ profiles to equation (E4) and to identify any systematic uncertainties, we have performed simulations of the reaction kinetics. The simulations use the detailed mechanism for the $\text{CH}_2\text{I} + \text{O}_2$ system described by Ting *et al.*,⁴⁷ implemented in the stochastic kinetics simulation program *Kinetiscope* (version 1.1.956.x64).⁵⁹ The complete mechanism and the rate constants for each reaction appropriate for our experimental conditions are compiled in Table S6 in the Supporting Information but the key reactions are summarized here. The initial reaction between $\text{CH}_2\text{I} + \text{O}_2$ displays pressure-dependent branching as outlined in reactions (R2a), (R2b), and (R2c), with relative quantum yields of 0.69, 0.04, and 0.27, respectively, at 67 Torr. Ting *et al.* do not directly assign the products of reaction 2b as $\text{HCHO} + \text{IO}$, but we chose to do so here based on previous work that found it necessary to describe the early-time IO concentrations. CH_2OO is removed via several reactions. The reverse of reaction (R2a), shown as reaction (R3a), regenerates CH_2I , although cycling is effectively over in the first $\sim 10 \mu\text{s}$ following photolysis, beyond which the CH_2OO concentration declines. There are two major loss processes for CH_2OO : self-reaction (R4) and reaction with I atoms, which can lead either to $\text{HCHO} + \text{IO}$ via reaction (R3b) or to the CH_2IO_2 adduct via reaction (R3c). IO is formed predominantly by the reactions of I atoms with either CH_2OO via reaction (R3b) or with the adduct CH_2IO_2 :



In turn, IO loss is driven by its self-reaction.

Figure 7 shows simulated $[\text{CH}_2\text{OO}]_t$ and $[\text{IO}]_t$ profiles where initial concentrations of $[\text{CH}_2\text{I}]_0 = [\text{I}]_0 = 4.0 \times 10^{13} \text{ cm}^{-3}$ and $[\text{O}_2]_0 = 2.1 \times 10^{17} \text{ cm}^{-3}$ were used. The simulations are compared to average experimental concentration profiles measured in the absence of any carbonyl reactant. The experimental data shown in Figure 7 correspond to background measurements made in the course of BiAc experiments – the analogous data for Ac experiments are shown in Figure S6 in the

Supporting Information. While the simulation reproduces the peak $[\text{CH}_2\text{OO}]$ concentration reasonably well the loss is slower than the experiment: analysis of the simulated $[\text{CH}_2\text{OO}]_t$ profile

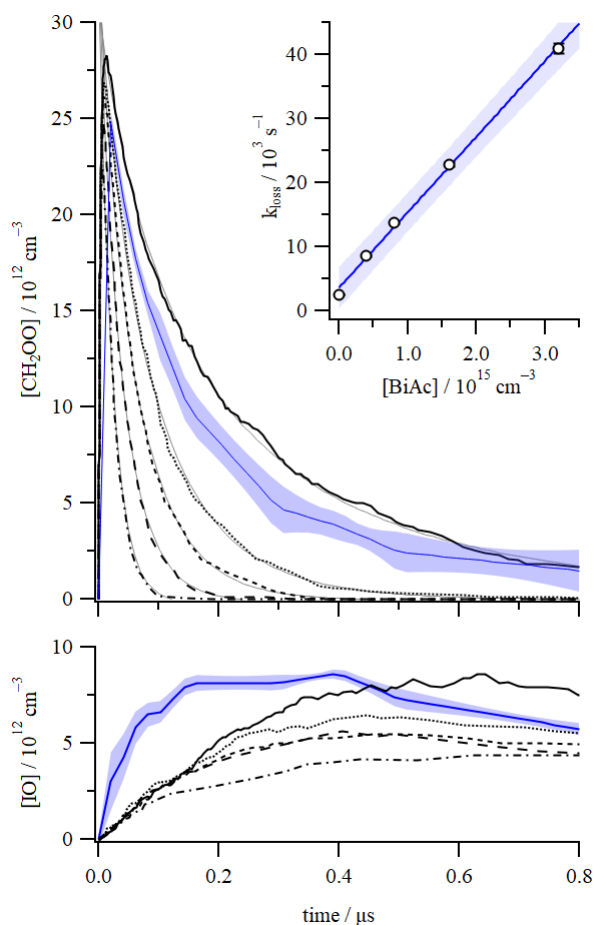


Figure 7 Simulated $[\text{CH}_2\text{OO}]_t$ and $[\text{IO}]_t$ profiles at various concentrations of BiAc: $[\text{BiAc}] / 10^{15} \text{ cm}^{-3} = 0$ (solid), 0.4 (dotted), 0.8 (short dash), 1.6, long dash), 3.2 (dash-dot). Average experimental profiles in the absence of BiAc are shown as blue lines with 1σ uncertainties shaded. Inset: pseudo-first order loss rates plotted as a function of $[\text{BiAc}]$ determined from analysis of simulated $[\text{CH}_2\text{OO}]_t$ profiles. Linear fit is shown with shaded area representing 2σ prediction band.

using equation (E5) yielded $k_{\text{bgd}} \approx 3000 \text{ s}^{-1}$. The simulated and experimental $[\text{IO}]_t$ profiles show similar discrepancies; maximum IO concentrations are in good agreement, but experimentally IO is

observed to form much more quickly.

The effect of an addition reactant for CIs was incorporated in the model by including an additional $\text{CH}_2\text{OO} + \text{X}$ reaction step. Simulations for the $\text{CH}_2\text{OO} + \text{BiAc}$ reaction using the experimental rate constant $k_{\text{BiAc}} = 1.4 \times 10^{-11} \text{ cm}^3 \text{ s}^{-1}$ and concentrations spanning the range $0.4 \times 10^{15} \text{ cm}^{-3}$ to $3.1 \times 10^{15} \text{ cm}^{-3}$, are also shown in Figure 7. The analogous simulations incorporating the $\text{CH}_2\text{OO} + \text{Ac}$ reaction using $k_{\text{Ac}} = 4.1 \times 10^{-13} \text{ cm}^3 \text{ s}^{-1}$ and concentrations in the range $0.5 \times 10^{16} \text{ cm}^{-3}$ to $4.0 \times 10^{16} \text{ cm}^{-3}$ are shown in Figure S6. For both reactions, the $[\text{CH}_2\text{OO}]_t$ profiles decay more rapidly as the reactant concentration is increased. The simulated $[\text{CH}_2\text{OO}]_t$ profiles were fit to equation (E5) to obtain k_{loss} as a function of $[\text{BiAc}]$ and $[\text{Ac}]$, which was then fit to equation (E4) to obtain k_X values. The pseudo-first order plots are shown in the insets to Figure 7 for BiAc and Figure S6 for Ac. Fitting the simulated data to equation (E4) returned bimolecular rate constants that were systematically lower than the values used in the model. For the faster BiAc reaction, analysis of the simulated $[\text{CH}_2\text{OO}]_t$ profiles returned a value of $k_{\text{BiAc,sim}} = (1.18 \pm 0.03) \times 10^{-11} \text{ cm}^3 \text{ s}^{-1}$, which is 86% of the input value used in the model. The discrepancy for the slower Ac reaction was smaller, with $k_{\text{Ac,sim}} = (3.8 \pm 0.2) \times 10^{-13} \text{ cm}^3 \text{ s}^{-1}$ being 93% of the input value. These results could imply that the analysis results in a modest systematic and k -dependent underestimation of the true bimolecular rate constants. Although, the simulations show several qualitative discrepancies from the experiments as will be discussed further below.

4. Computational results

Reaction Energetics: The reactions of Criegee intermediates with carbonyl compounds primarily occur through 1,3-cycloaddition across the carbonyl double bond leading to the formation of a cyclic secondary ozonide (SOZ).³³ Stationary points on this reaction pathway were identified at the M06-2X/aug-cc-pVTZ and CBS-QB3 levels of theory for reaction of CH_2OO with Ac (an aliphatic ketone), BiAc (a model α -diketone), and both the diketone (β -diketone) and enolone tautomers of AcAc. The

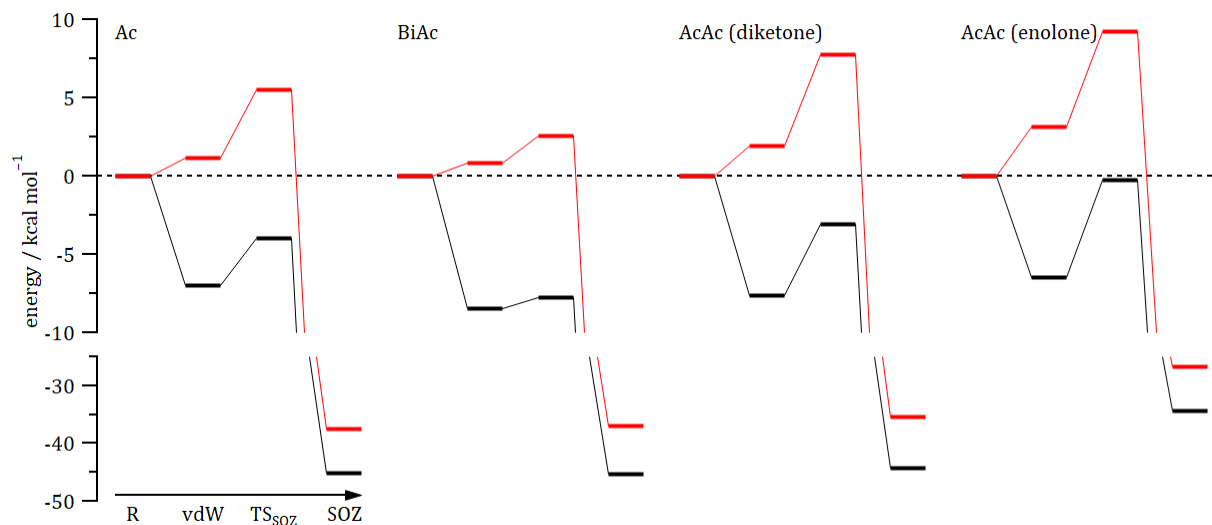


Figure 8 Stationary points on the potential energy surfaces for reactions of CH_2OO with representative carbonyls acetone (Ac), biacetyl (BiAc) and both diketone and enolone tautomers of acetylacetone (AcAc). Energies of reactants (R), entrance channel van der Waals complex (vdW), cycloaddition transition state (TS_{SOZ}), and secondary ozonide products (SOZ) are shown for each reaction. Energies were calculated at the CBS-QB3 level of theory (see Table 2) as described in the text. Free energies (ΔG ; 298 K) and zero-point corrected electronic energies ($\Delta E + \text{ZPE}$; 0 K) are shown in red and black, respectively.

energies calculated for reaction of CH_2OO with these chosen carbonyls are shown in Table 2 at the M06-2X/aug-cc-pVTZ and CBS-QB3 levels of theory. The reaction pathways are also illustrated in Figure 8 in terms of the changes in free energy (ΔG) at 298 K and the electronic energies at 0 K with zero-point energy (ZPE) correction ($\Delta E + \text{ZPE}$) calculated at the CBS-QB3 level of theory. Thermal corrections are calculated within the rigid rotor, harmonic oscillator (RRHO) approximation and inaccuracies due to incomplete treatment of low-frequency vibrations and hindered internal rotations are expected.

Table 2 Relative energies ($\Delta E + \text{ZPE}$ at 0 K), including zero-point contributions, and free energies (ΔG at 298 K), evaluated using RRHO partition functions, calculated at the M06-2X/aug-cc-pVTZ and CBS-QB3 levels for the SOZ pathway (see Figure 8) for reactions of CH_2OO with acetone (Ac), biacetyl (BiAc), and the enolone and diketone tautomers of acetylacetone (AcAc). All energies are reported in kcal mol^{-1} .

M06-2X/aVTZ	$\Delta E + \text{ZPE}$ ($\Delta G_{298 \text{ K}}$)		
	vdW	TS_{SOZ}	SOZ
Ac	-9.7 (0.7)	-6.8 (5.3)	-54.3 (-41.0)
BiAc	-10.7 (0.2)	-9.5 (2.7)	-54.1 (-41.4)
AcAc (keto)	-11.7 (0.2)	-5.7 (7.2)	-53.2 (-39.2)
AcAc (enol)	-8.1 (2.7)	-2.3 (9.5)	-41.6 (-28.9)
CBS-QB3	$\Delta E + \text{ZPE}$ ($\Delta G_{298 \text{ K}}$)		
	vdW	TS_{SOZ}	SOZ
Ac	-7.0 (1.2)	-4.0 (5.5)	-45.1 (-37.5)
BiAc	-8.4 (0.8)	-7.8 (2.5)	-45.3 (-37.0)
AcAc (keto)	-7.7 (1.9)	-3.1 (7.8)	-44.3 (-35.4)
AcAc (enol)	-6.5 (3.1)	-0.3 (9.2)	-34.4 (-26.8)

As can be seen in Figure 8, the cycloaddition reaction is initiated by the formation of a van der Waals entrance channel complex (vdW), typically stabilized at the zero-point level by $\sim 7\text{--}12 \text{ kcal mol}^{-1}$ with respect to the reactants. From the vdW minimum, the cycloaddition transition state (TS_{SOZ}) that leads to SOZ formation is higher in energy, but in all cases submerged relative to the separated reactants

in terms of the zero-point corrected electronic energies. The TS_{SOZ} complex is lower in energy by ~ 0 – 10 kcal mol^{-1} with respect to reactants depending on the carbonyl species and level of theory used. However, the entropic contribution to the free energy moves the relative energies of both the entrance channel complex and the transition state structure above the reactants by ~ 0 – 3 kcal mol^{-1} and ~ 3 – 10 kcal mol^{-1} , respectively (see Table 2). The formation of the SOZ is highly exoergic (ΔG ranges from $-27 \text{ kcal mol}^{-1}$ to $-41 \text{ kcal mol}^{-1}$), and this energized intermediate can undergo several further isomerization and decomposition reactions.³³ However, we do not characterize these subsequent reactions in detail as the cycloaddition reaction to form the SOZ will be most important in dictating the overall reaction kinetics, and the experimental technique used here is insensitive to the products formed.

Overall, both the M06-2X/aug-cc-pVTZ and CBS-QB3 levels of theory provide a similar picture of the energetics for the cycloaddition reaction pathway of CH_2OO to the carbonyls studied here. For acetone, the free energy of the transition state is $\sim 5 \text{ kcal mol}^{-1}$ above the separated reactants. The reaction of CH_2OO with acetone has been studied previously by Jalan, *et al.*,³³ however, only the $\Delta E + \text{ZPE}; 0 \text{ K}$ energies were reported. Using B3LYP geometries and electronic energies refined with RCCSD(T)-F12a, the electronic energies of the vdW and TS_{SOZ} complexes were calculated to be $-7.6 \text{ kcal mol}^{-1}$ and $-4.9 \text{ kcal mol}^{-1}$, respectively. These values are nearer to the CBS-QB3 values reported here. This should be expected though, as the CBS-QB3 composite method also utilizes B3LYP optimized geometries for subsequent coupled cluster calculations.⁴¹

For BiAc, both levels of theory predict a significantly lower free energy barrier of TS_{SOZ} of $\sim 2.5 \text{ kcal mol}^{-1}$ compared to an aliphatic ketone such as Ac. This is qualitatively consistent with the experimental results where α -diketones (BiAc and AcPr) have measured rate constants an order of magnitude larger than the other carbonyl species (see Table 1). This suggests that α -diketones in general undergo rapid cycloaddition reactions with Criegee intermediates. By contrast, both the enolone and diketone tautomers of AcAc have higher barriers to cycloaddition compared to acetone

and BiAc. In fact, TS_{SOZ} of the enolone tautomer, the dominant tautomer in the gas phase, has a calculated free energy of nearly 10 kcal mol⁻¹ above the separated reactants. This would indicate that the reaction rate for SOZ formation would be significantly slower for AcAc by comparison to Ac and BiAc.

In addition to the cycloaddition pathway characterized here, it is also possible for α,β -unsaturated carbonyls such as methacrolein (MACR) and methyl vinyl ketone (MVK) to undergo another cycloaddition reaction involving the carbonyl oxygen and the β -vinylic carbon leading to a seven-membered, cyclic adduct.²⁴ However, previous study of the reaction of CH₂OO with MACR and MVK using PIMS saw no evidence for the formation of these species and concluded that the reaction proceeds near exclusively through addition to the carbonyl C-O bond leading to the five-membered, cyclic SOZ.²⁴ Though this reaction is also possible for the enolone tautomer of AcAc, we do not calculate this alternative cycloaddition pathway given these previous observations.

With the results from Table 2, we can provide an estimate of the relative magnitudes for the rate constants of CH₂OO with carbonyls using a simplified, two-step model for the overall reaction rate.^{26,60,61} While we do not focus on this model here, the results have been included in the Supporting Information.

Frontier Molecular Orbitals: The reactions of CIs with carbonyl compounds are typically viewed as 1,3-dipolar cycloaddition reactions,⁶² where the CI is the 1,3-dipole and the carbonyl compound is the dipolarophile. The mechanism is analogous to a Diels-Alder reaction, which is achieved primarily through an interaction between the highest occupied molecular orbital (HOMO) of the electron rich species and the lowest unoccupied molecular orbital (LUMO) of the electron deficient species. In the case of forming the SOZ, the more electron rich carbonyl oxide would initiate bond formation via interaction of its HOMO with the π^* LUMO of the carbonyl.^{63,64}

The effects of carbonyl substituents on reactivity can be understood qualitatively using a model initially described by Sustmann,^{65,66} which considers the symmetry-allowed interactions of the molecular orbitals on each reactant and quantitatively using concepts from frontier molecular orbital theory.^{63,64} Figure 9 shows schematically the orbitals involved for the model $\text{CH}_2\text{OO} + \text{HCHO}$ reaction, based on Figure 1 from Sustmann.⁶⁵ Based on loose symmetry considerations, the CI π orbital

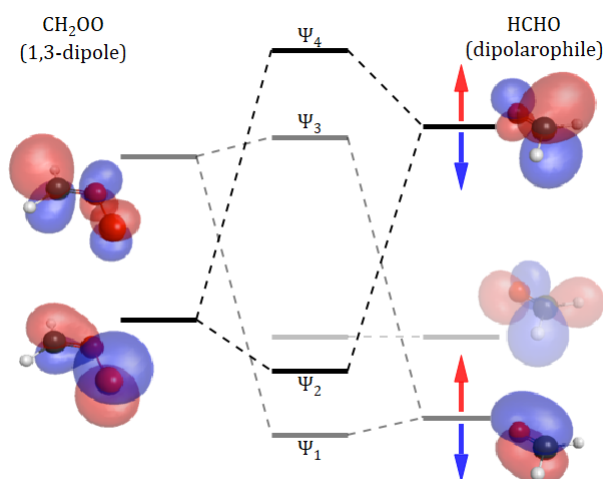


Figure 9 Schematic molecular orbital diagram, for the 1,3-dipolar cycloaddition reaction between CH_2OO and HCHO . Relative orbital energies are based on M06-2X/aug-cc-VTZ calculations. The “symmetric” combination (gray) has a large energy gap ΔE_S and gives rise to the Ψ_1 , Ψ_4 bonding and anti-bonding molecular orbitals. The “antisymmetric” combination (black) has a smaller energy gap ΔE_A and gives rise to the Ψ_2 , Ψ_3 pair. Red arrows: effect of electron-donating substituents; blue arrows: effect of electron-withdrawing substituents.

(HOMO) interacts with the π^* orbital (LUMO) of the carbonyl (“anti-symmetric”, $\Delta E_A = |\pi_{\text{CI}} - \pi^*_{\text{C=O}}|$), while the CI π^* orbital (LUMO) interacts with the π orbital (HOMO-1) of the carbonyls (“symmetric”, $\Delta E_S = |\pi^*_{\text{CI}} - \pi_{\text{C=O}}|$). The former energy gap ΔE_A is smaller than ΔE_S and this interaction makes the greater contribution to stabilizing the TS. Electron-withdrawing substituents on the carbonyl (dipolarophile) will lower the energies of the π^* and π orbitals, decreasing ΔE_A (stabilizing the TS) at

the expense of increasing the already larger value ΔE_S . In contrast, electron-donating substituents will raise the energies of the π^* and π orbitals, increasing ΔE_A and de-stabilizing the TS. Therefore, it would be expected that carbonyls with electron-withdrawing substituents would undergo more rapid cycloaddition with a given CI due to the smaller ΔE_A energy gap.

Table 3 Frontier orbital energies calculated at the M06-2X/aVTZ level.

	E_π / eV	E_{π^*} / eV	ΔE_A / eV	ΔE_S / eV
CH ₂ OO	-8.77	-1.65		
acetaldehyde (AcA)	-11.95	0.32	9.09	10.29
acetone (Ac)	-11.51	0.87	9.64	9.85
hexafluoroacetone (HFA)	-14.56	-1.86	6.91	12.91
biacetyl (BiAC)	-12.11	-1.30	7.47	10.46
acetylpropionyl (AcPr)	-12.09	-1.24	7.53	10.44
acetylacetone (AcAc, diketone)	-11.92	-0.42	8.35	10.27
acetylacetone (AcAc, enolone)	-11.72	-0.40	8.37	10.06
3,3-dimethyl-2,4-pentanedione (dMAcAc)	-11.60	-0.49	8.28	9.95
methylvinylketone (MVK)	-11.96	-0.78	7.99	10.31
methacrolein (MACR)	-12.65	-0.82	7.95	11.00

To explore these trends in more detail, the frontier orbital energies for the π and the π^* orbitals of the simplest CI (CH₂OO) and a range of carbonyls with known CI reaction rate constants were calculated at the M06-2X/aVTZ level of theory. These values are shown in Table 3 along with the corresponding values for ΔE_A and ΔE_S . For this analysis, only the π orbitals are considered; we neglect

any contribution from the non-bonding n_0 (HOMO) of the carbonyls. These results will be discussed further below with detailed comparison to the known CI reaction rate constants of each carbonyl.

Discussion

1. Systematic uncertainties in k_{loss}

Analysis of $[\text{CH}_2\text{OO}]_t$ profiles obtained from simulations using the detailed mechanism and rate constants for the $\text{CH}_2\text{I} + \text{O}_2$ reaction reported by Ting et al.⁴⁷ suggested that fitting to equation (E5) may lead to a possible systematic and k -dependent underestimation of the true bimolecular rate constants for the $\text{CH}_2\text{OO} + \text{X}$ reactions. For the faster reaction $\text{CH}_2\text{OO} + \text{BiAc}$, the rate constant was $\sim 84\%$ of the value used in the simulation, while a smaller discrepancy of $\sim 93\%$ was found for the slower $\text{CH}_2\text{OO} + \text{Ac}$ reaction. We note that the value of k_{Ac} (discussed below) is in good agreement with previous measurements although a correction for the systematic error implied by the modeling would increase it by only 7%, which is within the reported uncertainty. A greater increase of $\sim 19\%$ would be implied for the BiAc reaction rate constant. However, the model has sufficient deficiencies, which would suggest that any such correction is unjustified.

As has already been noted, the decay rate of CH_2OO and formation rate of IO in the absence of an additional reactant are both underpredicted when compared to the experimental data, although the peak concentrations are well-reproduced. Inclusion of BiAc or Ac reactions in the simulation leads to increased loss rates of CH_2OO , which were observed experimentally, but also decreased yields of IO, which were not. Within the reaction model, IO is formed by the reactions of I atoms with CH_2OO via reaction (R3b) or with CH_2IO_2 via reaction (R5). Increasing BiAc or Ac concentrations compete with I atoms for CH_2OO and reduce the contribution of reaction (R3b) to the IO yield. At the highest simulated reactant concentrations, maximum [IO] is reduced by around a factor of two relative to the background conditions, in contrast to the experiments, which show no noticeable effect on the $[\text{IO}]_t$.

profiles.

Neither rate constant for IO production used in the model has been measured directly. Ting *et al.*⁴⁷ report a value of $9.0 \times 10^{-12} \text{ cm}^3 \text{ s}^{-1}$ for reaction (R3b), although this value was adjusted significantly from a much smaller theoretical value of $5.5 \times 10^{-14} \text{ cm}^3 \text{ s}^{-1}$ to better describe early time IO formation. Similarly, the rate constant for reaction (R5) of $3.5 \times 10^{-11} \text{ cm}^3 \text{ s}^{-1}$ is taken directly from earlier estimates based on mechanisms that explicitly did not include the Criegee intermediate.^{67,68} Adjustment of these rate constants, or alternatively exclusion of existing reactions or inclusion of additional reactions could be used to bring the simulations into better agreement with the experimental observations across the range of reactant concentrations. However, it is unclear that such revisions would necessarily provide greater confidence that implied systematic uncertainties in the rate constants for the reactions of CH₂OO with additional reactants are real. The current experimental results do, however, suggest that IO production is effectively decoupled from CH₂OO loss. The initial branching fraction for reaction (R2a) appears to be in accord with the experimental observations and the maximum observed [IO] is consistent with the expected yield of the CH₂IO₂ adduct via reaction (R2b). A parsimonious explanation is that IO is formed near exclusively from conversion of the CH₂IO₂ adduct, likely via reaction (R5), although a significantly larger rate constant for this reaction would be necessary to account for the early time kinetics.

2. Previous measurements

Only the CH₂OO + Ac reaction has been studied previously. The rate constant determined in this work ($k_{\text{Ac}} = 4.1 \times 10^{-13} \text{ cm}^3 \text{ s}^{-1}$ at 295 K and 67 Torr) is in reasonably good agreement with previous measurements made at similar temperatures and pressures. Two previous measurements have used the same photochemical method to produce CH₂OO. A value of $2.3 \times 10^{-13} \text{ cm}^3 \text{ s}^{-1}$ was measured by Taatjes *et al.* at 293 K and 4 Torr while Elsamra *et al.* found a positive pressure dependence over 4–50 Torr and a rate constant of $3.5 \times 10^{-13} \text{ cm}^3 \text{ s}^{-1}$ at the upper end of the range at 298 K.^{21,23} The value

determined in the current work at 67 Torr lies on the trend suggested by the pressure-dependent measurements (see Figure S7), which is consistent with the conclusion of Elsamra et al. that their experimental conditions corresponded to the low pressure limit. The value of $3.4 \times 10^{-13} \text{ cm}^3 \text{ s}^{-1}$ reported by Berndt *et al.* was determined using ethene ozonolysis to produce CH_2OO in synthetic air at atmospheric pressure,²⁰ and agrees (within the mutual uncertainties) with the low-pressure measurements.

3. Mechanism and reactivity trends

The α -diketones BiAc and AcPr react much more rapidly with CH_2OO than acetone, with rate constants that are approximately 25 times larger ($k_{\text{BiAc}} = 1.45 \times 10^{-11} \text{ cm}^3 \text{ s}^{-1}$ and $k_{\text{AcPr}} = 1.29 \times 10^{-11} \text{ cm}^3 \text{ s}^{-1}$). The larger rate constants for the α -diketone reactions relative to that for acetone can be rationalized, at least qualitatively, by the results of the *ab initio* calculations. The free energy profiles calculated using the CBS-Q3 method are shown in Figure 8 for the Ac and BiAc reactions (see also Table 2) and indicate that the cycloaddition transition state (TS_{SOZ}) is $3.0 \text{ kcal mol}^{-1}$ lower for the latter reaction.

In contrast to the α -diketone reactions, the rate constants obtained for the reactions of the β -diketones AcAc and dMAcAc with CH_2OO are similar in magnitude ($k_{\text{AcAc}} = 6.6 \times 10^{-13} \text{ cm}^3 \text{ s}^{-1}$ and $k_{\text{dMAcAc}} = 3.5 \times 10^{-13} \text{ cm}^3 \text{ s}^{-1}$) to k_{Ac} . The picture is more complicated for the β -diketones due to tautomerization. For AcAc, the enolone form is strongly favored ($\sim 97\%$) in the gas phase at room temperature^{69,70} and the absorption spectrum of dMAcAc shows features that may indicate some degree of tautomerization. Focusing first on AcAc, Figure 8 shows the free energy profiles for SOZ production via the cycloaddition reaction for both diketone and enolone forms. The free energy barriers are higher than that for the benchmark Ac reaction for both tautomers (by $2.3 \text{ kcal mol}^{-1}$ higher for the minor diketone and $3.7 \text{ kcal mol}^{-1}$ for the major enolone form). Application of the Eyring equation would predict rate constants for the diketone that is ~ 50 and ~ 500 times smaller

than Ac reaction (see Supporting Information). Weighting for the relative abundances, the minor diketone tautomer accounts for one in four reactive encounters and an overall rate constant that is ~400 times smaller than that for Ac, while the experiment finds k_{Ac} to be ~20% larger than k_{dMAcAc} . The qualitative disagreement suggests that additional reaction pathways via the other functional groups (C=C and OH) in the enolone form may be available.

By comparison, rate constants for reactions of CH₂OO with alcohols are similar in magnitude ($k_{ROH} \approx 10^{-13} \text{ cm}^3 \text{ s}^{-1}$),^{25,26} while reactions with alkenes are significantly slower ($k_{C=C} \approx 10^{-15} \text{ cm}^3 \text{ s}^{-1}$).²⁹ The conjugated enone functionality is shared with methylvinylketone, which reacts with CH₂OO with a rate constant of $k_{MVK} = (5.0 \pm 0.2) \times 10^{-13} \text{ cm}^3 \text{ s}^{-1}$,²⁴ although the reaction occurs predominantly via cycloaddition at the carbonyl group to form the SOZ, rather than reacting at the C=C double bond. Detection of the products of the CH₂OO + AcAc reaction using techniques such as PIMS or FTIR would be valuable. For the CH₂OO + dMAcAc reaction, the smaller rate constant relative to CH₂OO + Ac is qualitatively consistent with the *ab initio* prediction of higher energy transition state barrier for the diketone, although steric hindrance due to the presence of methyl groups at the C3 position may also contribute. The equilibrium constant for dMAcAc tautomerization is unknown, but since it would have to involve a terminal C=C bond, it is likely to be disfavored in the absence of additional stabilization through conjugation and intramolecular H-bond formation as in AcAc.

Previously, Taatjes *et al.*²¹ used PIMS to study the reactions of CH₂OO with acetone (Ac), acetaldehyde (AcA), and hexafluoroacetone (HFA), confirming the formation of SOZ products (for the Ac and HFA reactions). The observed rate constant trend $k_{Ac} < k_{AcA} \ll k_{HFA}$ mirrored the trend in the electron-withdrawing character of the carbonyl substituents CH₃ < H << CF₃, which increasingly stabilize the transition state. Here, we demonstrate that reactivity trends can be predicted and explained by

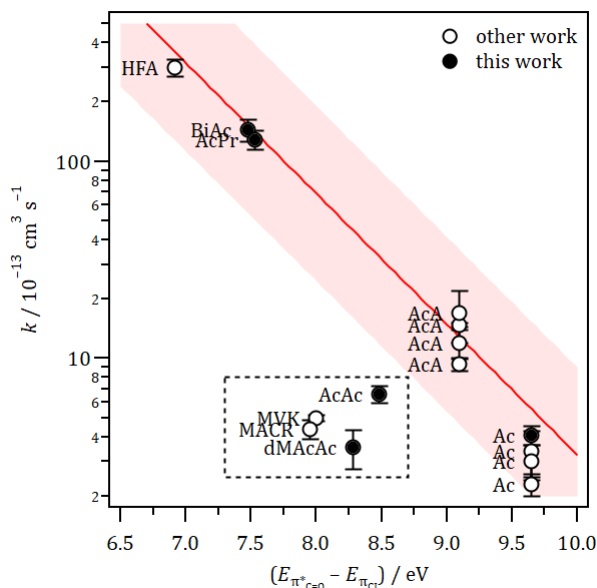


Figure 10 Inverse correlation between $\ln k$ and the energy gap between the carbonyl π^* orbital (LUMO) and the π orbital (HOMO) of CH₂OO. Orbital energies were calculated at the M06-2X/aVTZ level. Filled circles are measurements from this work, open circles are results of previous work. A linear fit with 2σ prediction band is shown ($R^2 = 0.83$). Reactions indicated in the dashed box were not included in the fit.

considering the influence of the substituents on the energies of the frontier orbitals of the dipolarophiles. Figure 10 shows a plot of $\ln k$ against ΔE_A (see Table 3) for a range of CH₂OO reactions with carbonyl and dicarbonyls. In general, we find a strong inverse correlation (the linear fit shown in Figure 10 has $R^2 = 0.83$) for CI reactions involving monocarbonyls (AcA, Ac, HFA) or α -diketones (BiAc, AcPr), however, the conjugated enones (MACR, MVK, AcAc) and the β -diketone dMAcAc

deviate from the trend and react more slowly than would be predicted. The relationship between $\ln k$ and ΔE_A can be used to estimate the rate constant for the simplest reaction of a Criegee intermediate with a given carbonyl. For instance, in the reaction of CH_2OO and HCHO , the orbital energy gap for this reaction is $\Delta E_{\text{FMO}} = 8.436$ eV (see Table 3), and based upon the linear fit and prediction bands shown in Figure 10, we estimate a rate constant of $(3.5_{-1.6}^{+2.9}) \times 10^{-12} \text{ cm}^3 \text{ s}^{-1}$.

An alternative approach to predict rate constants for the 1,3-dipolar cycloaddition reactions between CH_2OO and carbonyl compounds uses Hammett substituent constants which can be viewed as proxy measures of the degree of electron-withdrawing/electron-donating character of the substituents on the carbonyl.^{71,72} Here, we do not perform a standard Hammett analysis[†] but rather observe a strong positive correlation between the bimolecular rate constants and the sum of the *para* position Hammett substituent constant (σ_p) values for the substituents on the carbonyls. Figure 11 shows that a plot of k versus $\Sigma\sigma_p$ is linear with correlation coefficient $R^2 = 0.93$ – an equally large value is obtained using the *meta* position constants, σ_m . Substituent constants are taken from the work of Hansch *et al.*⁷² for the carbonyls Ac, AcA, MVK, MACR, BiAc, AcPr, and HFA and are compiled in Table S7. While there is an apparent ambiguity in the choice of substituents on the asymmetric α -diketone AcPr, which can be viewed as either CH_3 and $\text{C}(\text{O})\text{C}_2\text{H}_5$ or alternatively as C_2H_5 and $\text{C}(\text{O})\text{CH}_3$, the sums $\Sigma\sigma_p$ values are nearly the same in either case, and the correlation is largely unaffected. As with the frontier orbital analysis, this empirical correlation can be used to predict the gas phase rate constant for other reactions. For example, using the upper and lower prediction bounds in Figure 11 the rate constant for the $\text{CH}_2\text{OO} + \text{HCHO}$ reaction, for which $\Sigma\sigma_p = 0$, is estimated to be $(5.7 \pm 0.7) \times 10^{-12} \text{ cm}^3 \text{ s}^{-1}$.

[†] A standard Hammett analysis uses the relationship $\ln\left(\frac{k}{k_0}\right) = \sigma\rho$ where σ and ρ are the substituent and reaction constants, respectively, and k_0 is the rate constant for a reference reaction with $\sigma = 0$. For the current data set, a standard Hammett plot is non-linear.

¹ (1σ uncertainty), which is in good agreement with the FMO prediction.

The use of tabulated Hammett substituent constants may provide a quantitative means to predict rate constants for $\text{CH}_2\text{OO} + \text{carbonyl}$ reactions; where unavailable, relatively low-cost *ab initio* calculations of the relevant orbital energies may also provide a suitable substitute without the need to apply a full TST treatment. For instance, the rate constant for the reaction of the atmospherically important α -dicarbonyl glyoxal (Gly) with CH_2OO is predicted to be $(1.5 \pm 0.2) \times 10^{-11} \text{ cm}^3 \text{ s}^{-1}$. For the

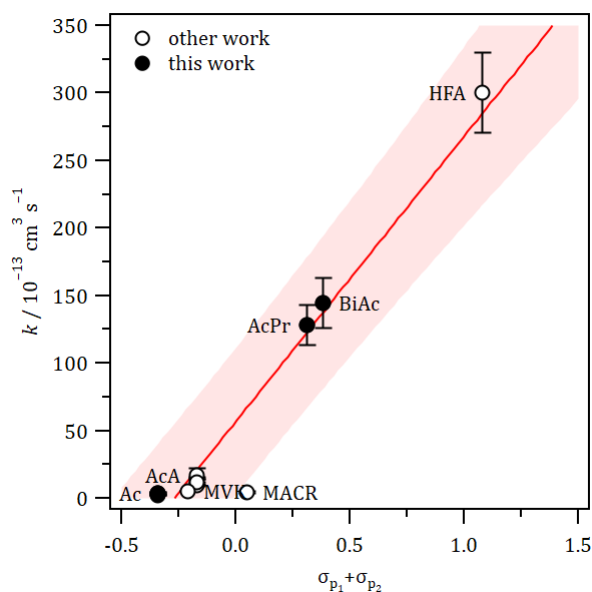


Figure 11 Plot showing correlation between observed rate constants and the sum of the *para* position Hammett constants, σ_p , for each substituent on the carbonyl. Closed circles are from this work, open circles are results of previous work. A linear fit with 2σ prediction band is shown ($R^2 = 0.93$).

related species methylglyoxal (MGly), we estimate rate constants of $(1.1 \pm 0.2) \times 10^{-11} \text{ cm}^3 \text{ s}^{-1}$ for reaction at the ketone and $(1.7 \pm 0.2) \times 10^{-11} \text{ cm}^3 \text{ s}^{-1}$ for reaction at the aldehyde group. Experimental work to measure the rate constants for the $\text{CH}_2\text{OO} + \text{Gly}$ and MGly reactions and test these predictions is underway.

4. Atmospheric implications

Acetone is typically found in the troposphere in low concentrations with mixing ratios of <2 ppb.⁷³ Dicarbonyls (BiAc, AcAc, Gly) have been detected at similar or even lower mixing ratios.⁷⁴⁻⁷⁷ Using 2 ppb as an upper limit, the rate constants measured (or estimated) in the current work indicate CH₂OO loss rates of <0.03 s⁻¹ for reaction with Ac or AcAc, and <0.6 s⁻¹ for reaction with BiAc or Gly. Consequently, reactions with acetone and dicarbonyl species are in general a negligible sink for CH₂OO in the troposphere where reaction with water vapor contributes a loss rate of ~2000 s⁻¹ at 50% RH.⁸ Reaction with CH₂OO (or other CIs) is also likely a very minor sink for the carbonyl/dicarbonyl compounds when compared to reaction with OH or photolysis. For example, Ac reacts slightly more slowly with OH (1.8×10⁻¹³ cm³ s⁻¹)^{57,78} than with CH₂OO, but the much larger concentration of OH (~10⁶ cm⁻³) compared to CH₂OO (~10⁴ cm⁻³)⁴ leads to the former reaction being around 30 times faster. For dicarbonyls too, reaction with OH is generally faster than reaction with CH₂OO. The rate constant for the OH + AcAc reaction is significantly larger (~9×10⁻¹¹ cm³ s⁻¹),^{46,76,79} while that for the OH + Gly reaction is similar in magnitude (1.1×10⁻¹¹ cm³ s⁻¹),⁷⁸ to the measured (or estimated) rate constants for the reactions with CH₂OO. Despite the reported rate constant for the OH + BiAc reaction being small (2.2×10⁻¹³ cm³ s⁻¹),⁸⁰ reaction with OH is still twice as fast as reaction with CH₂OO. For dicarbonyls in particular, photolysis is the dominant loss process in the troposphere. Photolysis rates of ~10⁴ s⁻¹ for the dicarbonyls (AcAc, BiAc, Gly) have been reported, which result in atmospheric lifetimes of only a few hours.^{46,74,81} The rate of photolysis of Ac is much slower (4×10⁻⁷ s⁻¹),⁸² but is still faster than reaction with either OH or CH₂OO. Considering all three processes, we estimate that reaction with CIs could be responsible for <1% of the loss of Ac and <0.1% for BiAc, AcAc, or Gly in the troposphere.

Conclusions

The rate constants for the 1,3-dipolar cycloaddition reactions of the Criegee intermediate CH₂OO with

acetone (Ac), two α -diketones (BiAc and AcPr), and two β -diketones (AcAc and dMAcAc) have been measured at a temperature of 295 K and a pressure of 67 Torr. The rate constant measured for the Ac reaction in this work [$k_{\text{Ac}} = (4.1 \pm 0.4) \times 10^{-13} \text{ cm}^3 \text{ s}^{-1}$] is in good agreement with previous measurements; acetone dimers may also contribute to reactivity at higher reactant concentrations. The α -diketones are significantly (~ 30 – 35 times) more reactive towards CH_2OO [$k_{\text{BiAc}} = (1.29 \pm 0.15) \times 10^{-11} \text{ cm}^3 \text{ s}^{-1}$ and $k_{\text{AcPr}} = (1.45 \pm 0.18) \times 10^{-11} \text{ cm}^3 \text{ s}^{-1}$] than Ac. The reactivity trends of carbonyl and dicarbonyl species towards CH_2OO can be explained using concepts from frontier molecular orbital theory – rate constants inversely correlate with the energy gap between the “antisymmetric” LUMO of the carbonyl and the HOMO of CH_2OO . The presence of electron-withdrawing groups lowers the energy of the carbonyl LUMO, leading to a smaller energy gap, while electron-donating substituents increase the energy gap. More simply, the rate constants correlate strongly with the electron-withdrawing/donating character of substituents quantified by Hammett parameters, which may provide a simple predictive approach for rate constants. The β -diketones show reactivity towards CH_2OO that is similar to that of acetone [$k_{\text{AcAc}} = (6.59 \pm 0.68) \times 10^{-13} \text{ cm}^3 \text{ s}^{-1}$ and $k_{\text{dMAcAc}} = (3.54 \pm 0.79) \times 10^{-13} \text{ cm}^3 \text{ s}^{-1}$], although the presence of enolone tautomers clouds the picture due to the presence of additional functional groups and the limited range of loss rates suggest that these rate constants may be better considered as upper limits. For the more atmospherically relevant carbonyl species, the rate constants are too small for these reactions to have a significant impact in the troposphere.

Acknowledgements

This material is based upon work supported by the National Science Foundation under Grant No. ECS-1905364. Financial support from the Undergraduate Research Opportunities Program (UROP) at the University of California, Irvine is gratefully acknowledged. Undergraduate researchers Altay Bayrakci, Terra Wang, Khanh Pham, Uyen Le, Duy Nguyen, and Reilly Carlton contributed to some of

the experiments. Finally, we thank Dr. Dmitry A. Fishman of the Laser Spectroscopy Facility for assistance with the UV/Vis absorption measurements.

Supporting Information

Pseudo-first^t order plots and overall, individual, and global fits and fit parameters; mechanism and rate constants for $\text{CH}_2\text{I} + \text{O}_2$ reaction; k_{Ac} pressure dependence; discussion of theoretical rate constants; tabulated Hammett substituent constants; *ab initio* optimized geometries.

References

- (1) Hatakeyama, S.; Akimoto, H. Reactions of Criegee Intermediates in the Gas Phase. *Res. Chem. Intermediat.* **1994**, *20* (3–5), 503–524. <https://doi.org/10.1163/156856794X00432>.
- (2) Johnson, D.; Marston, G. The Gas-Phase Ozonolysis of Unsaturated Volatile Organic Compounds in the Troposphere. *Chem. Soc. Rev.* **2008**, *37* (4), 699–716. <https://doi.org/10.1039/B704260B>.
- (3) Taatjes, C. A.; Shallcross, D. E.; Percival, C. J. Research Frontiers in the Chemistry of Criegee Intermediates and Tropospheric Ozonolysis. *Phys. Chem. Chem. Phys.* **2014**, *16* (5), 1704–1718. <https://doi.org/10.1039/C3CP52842A>.
- (4) Khan, M. A. H.; Percival, C. J.; Caravan, R. L.; Taatjes, C. A.; Shallcross, D. E. Criegee Intermediates and Their Impacts on the Troposphere. *Environ. Sci.: Processes Impacts* **2018**, *20* (3), 437–453. <https://doi.org/10.1039/C7EM00585G>.
- (5) Cox, R. A.; Ammann, M.; Crowley, J. N.; Herrmann, H.; Jenkin, M. E.; McNeill, V. F.; Mellouki, A.; Troe, J.; Wallington, T. J. Evaluated Kinetic and Photochemical Data for Atmospheric Chemistry: Volume VII – Criegee Intermediates. *Atmos. Chem. Phys.* **2020**, *20* (21), 13497–13519. <https://doi.org/10.5194/acp-20-13497-2020>.
- (6) Criegee, R. Mechanism of Ozonolysis. *Angew. Chem. Int. Ed.* **1975**, *14* (11), 745–752. <https://doi.org/10.1002/anie.197507451>.
- (7) Vereecken, L.; Novelli, A.; Taraborrelli, D. Unimolecular Decay Strongly Limits the Atmospheric Impact of Criegee Intermediates. *Phys. Chem. Chem. Phys.* **2017**, *19* (47), 31599–31612. <https://doi.org/10.1039/C7CP05541B>.
- (8) Chao, W.; Hsieh, J.-T.; Chang, C.-H.; Lin, J. J.-M. Direct Kinetic Measurement of the Reaction of the Simplest Criegee Intermediate with Water Vapor. *Science* **2015**, *347* (6223), 751–754. <https://doi.org/10.1126/science.1261549>.
- (9) Welz, O.; Eskola, A. J.; Sheps, L.; Rotavera, B.; Savee, J. D.; Scheer, A. M.; Osborn, D. L.; Lowe, D.; Murray Booth, A.; Xiao, P. *et al.* Rate Coefficients of C1 and C2 Criegee Intermediate Reactions with Formic and Acetic Acid Near the Collision Limit: Direct Kinetics Measurements and Atmospheric Implications. *Angew. Chem. Int. Ed.* **2014**, *126* (18), 4635–4638. <https://doi.org/10.1002/ange.201400964>.
- (10) Foreman, E. S.; Kapnas, K. M.; Murray, C. Reactions between Criegee Intermediates and the Inorganic Acids HCl and HNO₃: Kinetics and Atmospheric Implications. *Angew. Chem. Int. Ed.* **2016**, *55* (35), 10419–10422. <https://doi.org/10.1002/anie.201604662>.
- (11) Berndt, T.; Herrmann, H.; Kurtén, T. Direct Probing of Criegee Intermediates from Gas-Phase Ozonolysis Using Chemical Ionization Mass Spectrometry. *J. Am. Chem. Soc.* **2017**, *139* (38), 13387–13392. <https://doi.org/10.1021/jacs.7b05849>.
- (12) Chhantyal-Pun, R.; Rotavera, B.; McGillen, M. R.; Khan, M. A. H.; Eskola, A. J.; Caravan, R. L.; Blacker, L.; Tew, D. P.; Osborn, D. L.; Percival, C. J. *et al.* Criegee Intermediate Reactions with Carboxylic Acids: A Potential Source of Secondary Organic Aerosol in the Atmosphere. *ACS Earth Space Chem.* **2018**, *2* (8), 833–842. <https://doi.org/10.1021/acsearthspacechem.8b00069>.
- (13) Su, F.; Calvert, J. G.; Shaw, J. H. A FT IR Spectroscopic Study of the Ozone-Ethene Reaction Mechanism in Oxygen-Rich Mixtures. *J. Phys. Chem.* **1980**, *84* (3), 239–246. <https://doi.org/10.1021/j100440a003>.
- (14) Neeb, P.; Horie, O.; Moortgat, G. K. The Nature of the Transitory Product in the Gas-Phase Ozonolysis of Ethene. *Chem. Phys. Lett.* **1995**, *246* (1–2), 150–156. [https://doi.org/10.1016/0009-2614\(95\)01073-I](https://doi.org/10.1016/0009-2614(95)01073-I).
- (15) Neeb, P.; Horie, O.; Moortgat, G. K. Formation of Secondary Ozonides in the Gas-Phase Ozonolysis of Simple Alkenes. *Tetrahedron Lett.* **1996**, *37* (52), 9297–9300.

- [https://doi.org/10.1016/S0040-4039\(97\)82946-2](https://doi.org/10.1016/S0040-4039(97)82946-2).
- (16) Neeb, P.; Horie, O.; Moortgat, G. K. The Ethene–Ozone Reaction in the Gas Phase. *J. Phys. Chem. A* **1998**, *102* (34), 6778–6785. <https://doi.org/10.1021/jp981264z>.
- (17) Horie, O.; Schäfer, C.; Moortgat, G. K. High Reactivity of Hexafluoro Acetone toward Criegee Intermediates in the Gas-Phase Ozonolysis of Simple Alkenes. *Int. J. Chem. Kinet.* **1999**, *31* (4), 261–269. [https://doi.org/10.1002/\(SICI\)1097-4601\(1999\)31:4<261::AID-KIN3>3.0.CO;2-Z](https://doi.org/10.1002/(SICI)1097-4601(1999)31:4<261::AID-KIN3>3.0.CO;2-Z).
- (18) Fenske, J. D.; Hasson, A. S.; Ho, A. W.; Paulson, S. E. Measurement of Absolute Unimolecular and Bimolecular Rate Constants for CH₃CHOO Generated by the *trans*-2-Butene Reaction with Ozone in the Gas Phase. *J. Phys. Chem. A* **2000**, *104* (44), 9921–9932. <https://doi.org/10.1021/jp0016636>.
- (19) Tobias, H. J.; Ziemann, P. J. Kinetics of the Gas-Phase Reactions of Alcohols, Aldehydes, Carboxylic Acids, and Water with the C13 Stabilized Criegee Intermediate Formed from Ozonolysis of 1-Tetradecene. *J. Phys. Chem. A* **2001**, *105* (25), 6129–6135. <https://doi.org/10.1021/jp004631r>.
- (20) Berndt, T.; Kaethner, R.; Voigtländer, J.; Stratmann, F.; Pfeifle, M.; Reichle, P.; Sipilä, M.; Kulmala, M.; Olzmann, M. Kinetics of the Unimolecular Reaction of CH₂OO and the Bimolecular Reactions with the Water Monomer, Acetaldehyde and Acetone under Atmospheric Conditions. *Phys. Chem. Chem. Phys.* **2015**, *17* (30), 19862–19873. <https://doi.org/10.1039/C5CP02224J>.
- (21) Taatjes, C. A.; Welz, O.; Eskola, A. J.; Savee, J. D.; Osborn, D. L.; Lee, E. P. F.; Dyke, J. M.; Mok, D. W. K.; Shallcross, D. E.; Percival, C. J. Direct Measurement of Criegee Intermediate (CH₂OO) Reactions with Acetone, Acetaldehyde, and Hexafluoroacetone. *Phys. Chem. Chem. Phys.* **2012**, *14* (30), 10391–10400. <https://doi.org/10.1039/C2CP40294G>.
- (22) Stone, D.; Blitz, M.; Daubney, L.; Howes, N. U. M.; Seakins, P. Kinetics of CH₂OO Reactions with SO₂, NO₂, NO, H₂O and CH₃CHO as a Function of Pressure. *Phys. Chem. Chem. Phys.* **2014**, *16* (3), 1139–1149. <https://doi.org/10.1039/C3CP54391A>.
- (23) Elsamra, R. M. I.; Jalan, A.; Buras, Z. J.; Middaugh, J. E.; Green, W. H. Temperature- and Pressure-Dependent Kinetics of CH₂OO + CH₃COCH₃ and CH₂OO + CH₃CHO: Direct Measurements and Theoretical Analysis. *Int. J. Chem. Kinet.* **2016**, *48* (8), 474–488. <https://doi.org/10.1002/kin.21007>.
- (24) Eskola, A. J.; Döntgen, M.; Rotavera, B.; Caravan, R. L.; Welz, O.; Savee, J. D.; Osborn, D. L.; Shallcross, D. E.; Percival, C. J.; Taatjes, C. A. Direct Kinetics Study of CH₂OO + Methyl Vinyl Ketone and CH₂OO + Methacrolein Reactions and an Upper Limit Determination for CH₂OO + CO Reaction. *Phys. Chem. Chem. Phys.* **2018**, *20* (29), 19373–19381. <https://doi.org/10.1039/C8CP03606C>.
- (25) McGillen, M. R.; Curchod, B. F. E.; Chhantyal-Pun, R.; Beames, J. M.; Watson, N.; Khan, M. A. H.; McMahan, L.; Shallcross, D. E.; Orr-Ewing, A. J. Criegee Intermediate–Alcohol Reactions, A Potential Source of Functionalized Hydroperoxides in the Atmosphere. *ACS Earth Space Chem.* **2017**. <https://doi.org/10.1021/acsearthspacechem.7b00108>.
- (26) Tadayon, S. V.; Foreman, E. S.; Murray, C. Kinetics of the Reactions between the Criegee Intermediate CH₂OO and Alcohols. *J. Phys. Chem. A* **2018**, *122* (1), 258–268. <https://doi.org/10.1021/acs.jpca.7b09773>.
- (27) Osborn, D. L.; Taatjes, C. A. The Physical Chemistry of Criegee Intermediates in the Gas Phase. *Int. Rev. Phys. Chem.* **2015**, *34* (3), 309–360. <https://doi.org/10.1080/0144235X.2015.1055676>.
- (28) Taatjes, C. A. Criegee Intermediates: What Direct Production and Detection Can Teach Us About Reactions of Carbonyl Oxides. *Annu. Rev. Phys. Chem.* **2017**, *68* (1), 183–207. <https://doi.org/10.1146/annurev-physchem-052516-050739>.
- (29) Buras, Z. J.; Elsamra, R. M. I.; Jalan, A.; Middaugh, J. E.; Green, W. H. Direct Kinetic Measurements of Reactions between the Simplest Criegee Intermediate CH₂OO and Alkenes. *J. Phys. Chem. A*

- 2014**, *118* (11), 1997–2006. <https://doi.org/10.1021/jp4118985>.
- (30) Cremer, D.; Kraka, E.; McKee, M. L.; Radharkrishnan, T. P. The Carbonyl Oxide-Aldehyde Complex: A New Intermediate of the Ozonolysis Reaction. *Chem. Phys. Lett.* **1991**, *187* (5), 491–493. [https://doi.org/10.1016/0009-2614\(91\)80288-9](https://doi.org/10.1016/0009-2614(91)80288-9).
- (31) Aplincourt, P.; Ruiz-López, M. F. Theoretical Study of Formic Acid Anhydride Formation from Carbonyl Oxide in the Atmosphere. *J. Phys. Chem. A* **2000**, *104* (2), 380–388. <https://doi.org/10.1021/jp9928208>.
- (32) Aplincourt, P.; Ruiz-López, M. F. Theoretical Investigation of Reaction Mechanisms for Carboxylic Acid Formation in the Atmosphere. *J. Am. Chem. Soc.* **2000**, *122* (37), 8990–8997. <https://doi.org/10.1021/ja000731z>.
- (33) Jalan, A.; Allen, J. W.; Green, W. H. Chemically Activated Formation of Organic Acids in Reactions of the Criegee Intermediate with Aldehydes and Ketones. *Phys. Chem. Chem. Phys.* **2013**. <https://doi.org/10.1039/C3CP52598H>.
- (34) Foreman, E. S.; Kapnas, K. M.; Jou, Y.; Kalinowski, J.; Feng, D.; Gerber, R. B.; Murray, C. High Resolution Absolute Absorption Cross Sections of the \tilde{B}^1A' - \tilde{X}^1A' Transition of the CH₂OO Biradical. *Phys. Chem. Chem. Phys.* **2015**, *17* (48), 32539–32546. <https://doi.org/10.1039/C5CP04977F>.
- (35) Yaws, C. L. *The Yaws Handbook of Vapor Pressure*; Elsevier, 2015. <https://doi.org/10.1016/C2014-0-03590-3>.
- (36) Gaussian 16, Revision B.01, Frisch, M. J.; Trucks, G. W.; Schlegel, H. B.; Scuseria, G. E.; Robb, M. A.; Cheeseman, J. R.; Scalmani, G.; Barone, V.; Petersson, G. A.; Nakatsuji, H. *et al.* Gaussian, Inc., Wallingford CT, 2016.
- (37) Schmidt, M. W.; Baldridge, K. K.; Boatz, J. A.; Elbert, S. T.; Gordon, M. S.; Jensen, J. H.; Koseki, S.; Matsunaga, N.; Nguyen, K. A.; Su, S. *et al.* General Atomic and Molecular Electronic Structure System. *J. Comput. Chem.* **1993**, *14* (11), 1347–1363. <https://doi.org/10.1002/jcc.540141112>.
- (38) Gordon, M. S.; Schmidt, M. W. Advances in Electronic Structure Theory: GAMESS a Decade Later. In *Theory and Applications of Computational Chemistry, the First Forty Years*; Dykstra, C. E., Frenking, G., Kim, K. S., Scuseria, G. E., Eds.; Elsevier: Amsterdam, 2005; Vol. Chapter 41, pp 1167–1189.
- (39) Barca, G. M. J.; Bertoni, C.; Carrington, L.; Datta, D.; De Silva, N.; Deustua, J. E.; Fedorov, D. G.; Gour, J. R.; Gunina, A. O.; Guidez, E. *et al.* Recent Developments in the General Atomic and Molecular Electronic Structure System. *J. Chem. Phys.* **2020**, *152* (15), 154102. <https://doi.org/10.1063/5.0005188>.
- (40) Zhao, Y.; Truhlar, D. G. A New Local Density Functional for Main-Group Thermochemistry, Transition Metal Bonding, Thermochemical Kinetics, and Noncovalent Interactions. *J. Chem. Phys.* **2006**, *125* (19), 194101. <https://doi.org/10.1063/1.2370993>.
- (41) Montgomery, J. A.; Frisch, M. J.; Ochterski, J. W.; Petersson, G. A. A Complete Basis Set Model Chemistry. VI. Use of Density Functional Geometries and Frequencies. *J. Chem. Phys.* **1999**, *110* (6), 2822–2827. <https://doi.org/10.1063/1.477924>.
- (42) Xu, X.; Alecu, I. M.; Truhlar, D. G. How Well Can Modern Density Functionals Predict Internuclear Distances at Transition States? *J. Chem. Theory Comput.* **2011**, *7* (6), 1667–1676. <https://doi.org/10.1021/ct2001057>.
- (43) Schenker, S.; Schneider, C.; Tsogoeva, S. B.; Clark, T. Assessment of Popular DFT and Semiempirical Molecular Orbital Techniques for Calculating Relative Transition State Energies and Kinetic Product Distributions in Enantioselective Organocatalytic Reactions. *J. Chem. Theory Comput.* **2011**, *7* (11), 3586–3595. <https://doi.org/10.1021/ct2002013>.
- (44) Simmie, J. M.; Somers, K. P. Benchmarking Compound Methods (CBS-QB3, CBS-APNO, G3, G4, W1BD) against the Active Thermochemical Tables: A Litmus Test for Cost-Effective Molecular Formation Enthalpies. *J. Phys. Chem. A* **2015**, *119* (28), 7235–7246. <https://doi.org/10.1021/jp511403a>.

- (45) Keller-Rudek, H.; Moortgat, G. K.; Sander, R.; Sørensen, R. The MPI-Mainz UV/VIS Spectral Atlas of Gaseous Molecules of Atmospheric Interest. *Earth Syst. Sci. Data* **2013**, *5*, 365–373. <https://doi.org/10.5194/essd-5-365-2013>.
- (46) Messaadia, L.; El Dib, G.; Ferhati, A.; Chakir, A. UV-Visible Spectra and Gas-Phase Rate Coefficients for the Reaction of 2,3-Pentanedione and 2,4-Pentanedione with OH Radicals. *Chem. Phys. Lett.* **2015**, *626*, 73–79. <https://doi.org/10.1016/j.cplett.2015.02.032>.
- (47) Ting, W.-L.; Chang, C.-H.; Lee, Y.-F.; Matsui, H.; Lee, Y.-P.; Lin, J. J.-M. Detailed Mechanism of the $\text{CH}_2\text{I} + \text{O}_2$ Reaction: Yield and Self-Reaction of the Simplest Criegee Intermediate CH_2OO . *J. Chem. Phys.* **2014**, *141* (10), 104308. <https://doi.org/10.1063/1.4894405>.
- (48) Eskola, A. J.; Wojcik-Pastuszka, D.; Ratajczak, E.; Timonen, R. S. Kinetics of the Reactions of CH_2Br and CH_2I Radicals with Molecular Oxygen at Atmospheric Temperatures. *Phys. Chem. Chem. Phys.* **2006**, *8* (12), 1416–1424. <https://doi.org/10.1039/b516291b>.
- (49) Huang, Y.-H.; Chen, L.-W.; Lee, Y.-P. Simultaneous Infrared Detection of the ICH_2OO Radical and Criegee Intermediate CH_2OO : The Pressure Dependence of the Yield of CH_2OO in the Reaction $\text{CH}_2\text{I} + \text{O}_2$. *J. Phys. Chem. Lett.* **2015**, *6* (22), 4610–4615. <https://doi.org/10.1021/acs.jpcclett.5b02298>.
- (50) Foreman, E. S.; Murray, C. Kinetics of IO Production in the $\text{CH}_2\text{I} + \text{O}_2$ Reaction Studied by Cavity Ring-Down Spectroscopy. *J. Phys. Chem. A* **2015**, *119* (34), 8981–8990. <https://doi.org/10.1021/acs.jpca.5b05058>.
- (51) Su, Y.-T.; Lin, H.-Y.; Putikam, R.; Matsui, H.; Lin, M. C.; Lee, Y.-P. Extremely Rapid Self-Reaction of the Simplest Criegee Intermediate CH_2OO and Its Implications in Atmospheric Chemistry. *Nat. Chem.* **2014**, *6* (6), 477–483. <https://doi.org/10.1038/nchem.1890>.
- (52) Buras, Z. J.; Elsamra, R. M. I.; Green, W. H. Direct Determination of the Simplest Criegee Intermediate (CH_2OO) Self Reaction Rate. *J. Phys. Chem. Lett.* **2014**, *5* (13), 2224–2228. <https://doi.org/10.1021/jz5008406>.
- (53) Chhantyal-Pun, R.; Davey, A.; Shallcross, D. E.; Percival, C. J.; Orr-Ewing, A. J. A Kinetic Study of the CH_2OO Criegee Intermediate Self-Reaction, Reaction with SO_2 and Unimolecular Reaction Using Cavity Ring-down Spectroscopy. *Phys. Chem. Chem. Phys.* **2015**, *17* (5), 3617–3626. <https://doi.org/10.1039/C4CP04198D>.
- (54) Sheps, L. Absolute Ultraviolet Absorption Spectrum of a Criegee Intermediate CH_2OO . *J. Phys. Chem. Lett.* **2013**, *4* (24), 4201–4205. <https://doi.org/10.1021/jz402191w>.
- (55) Ting, W.-L.; Chen, Y.-H.; Chao, W.; Smith, M. C.; Lin, J. J.-M. The UV Absorption Spectrum of the Simplest Criegee Intermediate CH_2OO . *Phys. Chem. Chem. Phys.* **2014**, *16* (22), 10438–10443. <https://doi.org/10.1039/C4CP00877D>.
- (56) Spietz, P.; Gómez Martín, J. C.; Burrows, J. P. Spectroscopic Studies of the I_2/O_3 Photochemistry: Part 2. Improved Spectra of Iodine Oxides and Analysis of the IO Absorption Spectrum. *J. Photochem. Photobiol. A* **2005**, *176* (1–3), 50–67. <https://doi.org/10.1016/j.jphotochem.2005.08.023>.
- (57) J. B. Burkholder, S. P. Sander, J. Abbatt, J. R. Barker, C. Cappa, J. D. Crouse, T. S. Dibble, R. E. Huie, C. E. Kolb, M. J. Kurylo *et al.* “Chemical Kinetics and Photochemical Data for Use in Atmospheric Studies, Evaluation No. 19,” JPL Publication 19-5, Jet Propulsion Laboratory, Pasadena, 2019 <http://jpldataeval.jpl.nasa.gov>; 19; 2020.
- (58) Anderson, L. N.; Kudchadker, A. P.; Eubank, P. T. Volumetric Properties of Gaseous Acetone. *J. Chem. Eng. Data* **1968**, *13* (3), 321–327. <https://doi.org/10.1021/je60038a007>.
- (59) Hinsberg, W. D.; Houle, F. A. Kinetiscope - A stochastic kinetics simulator <https://hinsberg.net/kinetiscope/index.html> (accessed 2021 -08 -12).
- (60) Watson, N. A. I.; Black, J. A.; Stonelake, T. M.; Knowles, P. J.; Beames, J. M. An Extended Computational Study of Criegee Intermediate-Alcohol Reactions. *J. Phys. Chem. A* **2019**, *123* (1), 218–229. <https://doi.org/10.1021/acs.jpca.8b09349>.
- (61) Aroeira, G. J. R.; Abbott, A. S.; Elliott, S. N.; Turney, J. M.; Schaefer, H. F. The Addition of Methanol

- to Criegee Intermediates. *Phys. Chem. Chem. Phys.* **2019**, *21* (32), 17760–17771. <https://doi.org/10.1039/C9CP03480C>.
- (62) Bunnelle, W. H. Preparation, Properties, and Reactions of Carbonyl Oxides. *Chem. Rev.* **1991**, *91* (3), 335–362. <https://doi.org/10.1021/cr00003a003>.
- (63) Houk, K. N. Frontier Molecular Orbital Theory of Cycloaddition Reactions. *Acc. Chem. Res.* **1975**, *8* (11), 361–369. <https://doi.org/10.1021/ar50095a001>.
- (64) Fukui, K. Role of Frontier Orbitals in Chemical Reactions. *Science* **1982**, *218* (4574), 747–754. <https://doi.org/10.1126/science.218.4574.747>.
- (65) Sustmann, R. A Simple Model for Substituent Effects in Cycloaddition Reactions. I. 1,3-Dipolar Cycloadditions. *Tetrahedron Lett.* **1971**, *12* (29), 2717–2720. [https://doi.org/10.1016/S0040-4039\(01\)96961-8](https://doi.org/10.1016/S0040-4039(01)96961-8).
- (66) Sustmann, R. A Simple Model for Substituent Effects in Cycloaddition Reactions. II. The Diels-Alder Reaction. *Tetrahedron Lett.* **1971**, *12* (29), 2721–2724. [https://doi.org/10.1016/S0040-4039\(01\)96962-X](https://doi.org/10.1016/S0040-4039(01)96962-X).
- (67) Sehested, J.; Ellermann, T.; Nielsen, O. J. A Spectrokinetic Study of CH₂I and CH₂IO₂ Radicals. *Int. J. Chem. Kinet.* **1994**, *26* (2), 259–272. <https://doi.org/10.1002/kin.550260204>.
- (68) Gravestock, T. J.; Blitz, M. A.; Bloss, W. J.; Heard, D. E. A Multidimensional Study of the Reaction CH₂I + O₂: Products and Atmospheric Implications. *ChemPhysChem* **2010**, *11* (18), 3928–3941. <https://doi.org/10.1002/cphc.201000575>.
- (69) Nakanishi, H.; Morita, H.; Nagakura, S. Charge-Transfer Character in the Intramolecular Hydrogen Bond: Vacuum Ultraviolet Spectra of Acetylacetone and Its Fluoro Derivatives. *Bull. Chem. Soc. Jpn.* **1978**, *51* (6), 1723–1729. <https://doi.org/10.1246/bcsj.51.1723>.
- (70) Antonov, I.; Voronova, K.; Chen, M.-W.; Sztáray, B.; Hemberger, P.; Bodi, A.; Osborn, D. L.; Sheps, L. To Boldly Look Where No One Has Looked Before: Identifying the Primary Photoproducts of Acetylacetone. *J. Phys. Chem. A* **2019**, *123* (26), 5472–5490. <https://doi.org/10.1021/acs.jpca.9b04640>.
- (71) Hammett, L. P. The Effect of Structure upon the Reactions of Organic Compounds. Benzene Derivatives. *J. Am. Chem. Soc.* **1937**, *59* (1), 96–103. <https://doi.org/10.1021/ja01280a022>.
- (72) Hansch, Corwin.; Leo, A.; Taft, R. W. A Survey of Hammett Substituent Constants and Resonance and Field Parameters. *Chem. Rev.* **1991**, *91* (2), 165–195. <https://doi.org/10.1021/cr00002a004>.
- (73) Khan, M. A. H.; Cooke, M. C.; Utembe, S. R.; Archibald, A. T.; Maxwell, P.; Morris, W. C.; Xiao, P.; Derwent, R. G.; Jenkin, M. E.; Percival, C. J. *et al.* A Study of Global Atmospheric Budget and Distribution of Acetone Using Global Atmospheric Model STOCHEM-CRI. *Atmos. Environ.* **2015**, *112*, 269–277. <https://doi.org/10.1016/j.atmosenv.2015.04.056>.
- (74) Klotz, B.; Graedler, F.; Sørensen, S.; Barnes, I.; Becker, K.-H. A Kinetic Study of the Atmospheric Photolysis of α -Dicarbonyls. *Int. J. Chem. Kinet.* **2001**, *33* (1), 9–20. [https://doi.org/10.1002/1097-4601\(20010101\)33:1<9::AID-KIN2>3.0.CO;2-V](https://doi.org/10.1002/1097-4601(20010101)33:1<9::AID-KIN2>3.0.CO;2-V).
- (75) Volkamer, R.; Molina, L. T.; Molina, M. J.; Shirley, T.; Brune, W. H. DOAS Measurement of Glyoxal as an Indicator for Fast VOC Chemistry in Urban Air. *Geophys. Res. Lett.* **2005**, *32* (8). <https://doi.org/10.1029/2005GL022616>.
- (76) Zhou, S.; Barnes, I.; Zhu, T.; Bejan, I.; Albu, M.; Benter, T. Atmospheric Chemistry of Acetylacetone. *Environ. Sci. Technol.* **2008**, *42* (21), 7905–7910. <https://doi.org/10.1021/es8010282>.
- (77) Ji, Y.; Zheng, J.; Qin, D.; Li, Y.; Gao, Y.; Yao, M.; Chen, X.; Li, G.; An, T.; Zhang, R. OH-Initiated Oxidation of Acetylacetone: Implications for Ozone and Secondary Organic Aerosol Formation. *Environ. Sci. Technol.* **2018**, *52* (19), 11169–11177. <https://doi.org/10.1021/acs.est.8b03972>.
- (78) Atkinson, R.; Baulch, D. L.; Cox, R. A.; Crowley, J. N.; Hampson, R. F.; Hynes, R. G.; Jenkin, M. E.; Rossi, M. J.; Troe, J.; IUPAC Subcommittee. Evaluated Kinetic and Photochemical Data for Atmospheric Chemistry: Volume II – Gas Phase Reactions of Organic Species. *Atmos. Chem.*

- Phys.* **2006**, 6 (11), 3625–4055. <https://doi.org/10.5194/acp-6-3625-2006>.
- (79) Holloway, A.-L.; Treacy, J.; Sidebottom, H.; Mellouki, A.; Daële, V.; Bras, G. L.; Barnes, I. Rate Coefficients for the Reactions of OH Radicals with the Keto/Enol Tautomers of 2,4-Pentanedione and 3-Methyl-2,4-Pentanedione, Allyl Alcohol and Methyl Vinyl Ketone Using the Enols and Methyl Nitrite as Photolytic Sources of OH. *J. Photochem. Photobio. A* **2005**, 176 (1–3), 183–190. <https://doi.org/10.1016/j.jphotochem.2005.08.031>.
- (80) Dagaut, P.; Wallington, T. J.; Liu, R.; Kurylo, M. J. A Kinetic Investigation of the Gas-Phase Reactions of Hydroxyl Radicals with Cyclic Ketones and Diones: Mechanistic Insights. *J. Phys. Chem.* **1988**, 92 (15), 4375–4377. <https://doi.org/10.1021/j100326a026>.
- (81) Tadić, J.; Moortgat, G. K.; Wirtz, K. Photolysis of Glyoxal in Air. *J. Photochem. Photobio. A* **2006**, 177 (2), 116–124. <https://doi.org/10.1016/j.jphotochem.2005.10.010>.
- (82) Lee, K. L. K.; Nauta, K.; Kable, S. H. Photodissociation of Acetone from 266 to 312 nm: Dynamics of CH₃ + CH₃CO Channels on the S₀ and T₁ States. *J. Chem. Phys.* **2017**, 146 (4), 044304. <https://doi.org/10.1063/1.4974035>.

TOC graphic

